J. Fluid Mech. (2001), *vol.* 448, *pp.* 243–278.
DOI: 10.1017/S0022112001005936 Printed in the United Kingdom

Moderate-Reynolds-number flows in ordered and random arrays of spheres

By REGHAN J. HILL[1], DONALD L. KOCH[1] AND ANTHONY J. C. LADD[2]

[1]School of Chemical Engineering, Cornell University, Ithaca, NY 14853, USA

[2]Department of Chemical Engineering, University of Florida, Gainesville, FL 32611, USA

(Received 3 January 2001 and in revised form 4 June 2001)

Lattice-Boltzmann simulations are used to examine the effects of fluid inertia, at moderate Reynolds numbers, on flows in simple cubic, face-centred cubic and random arrays of spheres. The drag force on the spheres, and hence the permeability of the arrays, is calculated as a function of the Reynolds number at solid volume fractions up to the close-packed limits of the arrays. At Reynolds numbers up to $O(10^2)$, the non-dimensional drag force has a more complex dependence on the Reynolds number and the solid volume fraction than suggested by the well-known Ergun correlation, particularly at solid volume fractions smaller than those that can be achieved in physical experiments. However, good agreement is found between the simulations and Ergun's correlation at solid volume fractions approaching the close-packed limit. For ordered arrays, the drag force is further complicated by its dependence on the direction of the flow relative to the axes of the arrays, even though in the absence of fluid inertia the permeability is isotropic. Visualizations of the flows are used to help interpret the numerical results. For random arrays, the transition to unsteady flow and the effect of moderate Reynolds numbers on hydrodynamic dispersion are discussed.

1. Introduction

In the accompanying paper (Hill, Koch & Ladd 2001), we examined the first effects of fluid inertia on flows in ordered and random arrays of spheres. The small inertial correction to the Stokes-flow drag force on the spheres was shown to be proportional to the cube of the average fluid velocity. This scaling contrasts with the quadratic dependence to be expected at larger Reynolds numbers from typical scaling arguments and experimental studies of flow in porous media. In this work, we use lattice-Boltzmann simulations to examine the transition from small- to moderate-Reynolds-number flow in ordered and random arrays of spheres. Reynolds numbers up to $O(100)$ are achieved. For close-packed random arrays, the simulations are compared to experimental results in the literature.

Simulations of flows in fixed beds of spheres with solid volume fractions below the close-packed limit are helpful for understanding how fluid inertia affects sedimenting suspensions and fluidized beds, especially those for which the Stokes number is large. This motivates our examination of flows in fixed beds of spheres with relatively small solid volume fractions. From the simulations presented in this work, we obtain an empirical equation for the rate at which the average drag force on the spheres in fixed random arrays increases with the Reynolds number. This correlation is valid for solid

volume fractions in the range 0.1–0.64, and may be applicable to high-Stokes-number sedimenting suspensions and fluidized beds, when the Reynolds number based on the mean settling velocity is in the approximate range 30–100. We also examine, in some detail, flows in *ordered* arrays of spheres to help understand the inertial hydrodynamic interactions in *random* arrays. The relatively simple geometry of simple cubic and face-centred cubic arrays allows the topology of the flow fields to be easily visualized when the flow is directed along planes of symmetry.

Visualizing the flows not only helps to interpret the numerical results – for the dependence of the drag force on the Reynolds number and the solid volume fraction, for example – but also helps to explain how the fluid velocity field, modified by the effects of fluid inertia, may affect hydrodynamic dispersion at large Péclet numbers. Regions of fluid bounded by closed streamlines, for example, have been shown by Koch & Brady (1985) to make a *hold-up* contribution to the overall effective hydrodynamic diffusivity of a passive tracer that is $O(Pe^2)$ larger than the molecular diffusivity when $Pe \gg 1$. Here, $Pe = |\langle \boldsymbol{u} \rangle| a/D_m = Re\, v/D_m$ is the Péclet number, where D_m is the molecular diffusivity of the tracer in the fluid. In contrast, the dispersion due to open streamlines in random arrays, and off-axis flows in ordered arrays of spheres, grows much more slowly with the Péclet number (Koch & Brady 1989). Therefore, identifying the presence of recirculating flow at finite Reynolds numbers will indicate, at least qualitatively, to what extent hold-up dispersion may affect the effective hydrodynamic diffusivity.

The complex geometry of porous media and the nonlinear term in the Navier–Stokes equations make the theoretical and computational analysis of moderate-Reynolds-number flows particularly difficult. For randomly packed beds of particles, the dependence of the non-dimensional drag force, F, on the Reynolds number, Re, and the solid volume fraction, c, has been established experimentally, with an accuracy that is adequate for engineering design purposes. Perhaps the most well-known formula for predicting the pressure drop in randomly packed beds is the Ergun correlation (Ergun 1952).

Ergun's correlation is based on the approximation that the drag force on the particles in randomly packed beds is equal to the sum of a viscous force, proportional to the average velocity, and an inertial force, proportional to the square of the average velocity. The coefficients of these terms depend on the solid volume fraction, and the particle shape and size distributions. For a monodisperse packed bed of spheres, Ergun's correlation can be written in the form

$$F = 8.33c/(1-c)^3 + 0.18Re/(1-c)^3, \tag{1}$$

where the first term on the right-hand side has the same form as the well-known Carman correlation (Carman 1937) for Stokes flow in randomly packed beds of spheres. Note that the leading coefficient in the Carman correlation is 10.0 rather than 8.33, and hence Ergun's correlation necessarily under-predicts the Stokes-flow drag force by approximately 17%. This is presumably to achieve a better fit of the correlation to experimental results at finite Reynolds numbers. Details of Ergun's experiments will be elaborated below, but first we review more recent numerical and experimental studies of moderate-Reynolds-number flows in porous media.

Numerical simulations have helped in understanding the effects of fluid inertia on flows in two-dimensional porous media (Rojas & Koplik 1998; Andrade *et al.* 1997; Ghaddar 1995; Edwards *et al.* 1990; Eidsath *et al.* 1983). Koch & Ladd (1997) used a lattice-Boltzmann method to facilitate a comprehensive study of transverse flows in two-dimensional ordered and random arrays of aligned cylinders. At moderate

Reynolds numbers, when the flow is directed along the primary axis of a square array of cylinders, recirculating flow in the gaps between the cylinders significantly reduces the inertial (form drag) contribution to the total drag force. Under these conditions, the non-dimensional drag force increases relatively slowly with the Reynolds number. However, when the average pressure gradient is directed away from the primary axis, recirculating flow is unable to span the gaps between the cylinders. Under these conditions, the non-dimensional drag force increases much more rapidly with the Reynolds number, because the largest contribution to the drag force is due to fluid inertia.

Simulations of three-dimensional finite-Reynolds-number flows in porous media have been performed only for limited ranges of the solid volume fraction and the Reynolds number. Maier *et al.* (1998) performed lattice-Boltzmann simulations of Stokes flows and finite-Reynolds-number flows in randomly packed beds of spheres. The permeability of a cylindrical randomly packed bed of spheres with a solid volume fraction of 0.568 (packing P1 in their paper) was calculated at six Reynolds numbers up to approximately 6. Although they did not compare the dependence of the permeability on the Reynolds number with Ergun's correlation, their results suggest that $F = 68.6 + 0.500Re^2$ when $Re < 2$ and $F = 66.9 + 1.68Re$ when $2 < Re < 6$, whereas Ergun's correlation at this solid volume fraction gives $F = 58.7 + 2.23Re$. The large difference between the coefficient of Re obtained from these simulations and Ergun's correlation have yet to be explained. Note that, in the absence of fluid inertia, Maier *et al.*'s simulations are in good agreement with $F = 70.5$ given by the Carman correlation at this solid volume fraction. We will see that the apparent discrepancy at finite Reynolds numbers is not due to inaccurately computing the effects of fluid inertia. Instead, we find that the difference is due to the increased sensitivity of the average drag force to the microstructure of the underlying sphere packing.

It is interesting to note that the form of Ergun's equation, as written above, suggests that at large solid volume fractions the transition from Re^2 to Re scaling occurs over a small range of Reynolds numbers. This is not necessarily true at small solid volume fractions, as might be concluded when considering the case of a single sphere in an unbounded fluid. In this case, the flow topology continues to develop with increasing Reynolds number, and F does not increase linearly with Re in any range of moderate Reynolds numbers (Clift, Grace & Weber 1978). This suggests that the range of Reynolds numbers where the inertial contribution to F undergoes a transition from Re^2 to Re scaling must diminish with increasing solid volume fraction. As discussed below, and demonstrated by the results presented in later sections, such a transition may be associated with a changing flow topology.

Inertial wakes behind the spheres in dilute random arrays cannot extend further than an $O(ac^{-1})$ distance downstream without being obstructed by another sphere. This is not the case for dilute *simple cubic* arrays, because, for certain directions of the flow, the wakes may extend much further downstream. Nevertheless, when the wakes are obstructed by downstream spheres, the velocity field may be expected to remain approximately self-similar with increasing Reynolds number, particularly at larger solid volume fractions. Then, since according to Bernoulli's equation pressure differences at large Reynolds numbers scale with the square of the average velocity, the non-dimensional drag force would increase linearly with the Reynolds number, which is indeed what Ergun's correlation suggests. However, as the distance between the spheres decreases, smaller Reynolds numbers would be required for a self-similar velocity field to develop, and hence the range of Reynolds numbers where the transition occurs would diminish with increasing solid volume fraction. The simulation results presented in this work show that this is indeed the case.

More recently, Fand *et al.* (1987) measured the permeability of a cylindrical packed bed of approximately monodisperse spheres at Reynolds numbers up to approximately 200. Their results confirm the transition from a Re^2 to Re dependence of the inertial contribution to F at small Reynolds numbers. At larger Reynolds numbers, they find $F = 145 + 4.70Re$ for $2.5 < Re < 40$ and $F = 156 + 4.62Re$ when $Re > 60$. The decrease in the coefficient of Re, which occurs in the range of Reynolds numbers 40–60, was attributed to the onset of unsteady flow, although they did not mention how or whether unsteady flow was actually identified. Nevertheless, the coefficient of Re at Reynolds numbers where F increases linearly with Re is almost 20% greater than given by Ergun's correlation, which at this solid volume fraction gives $F = 118 + 3.96Re$. Note that Carman's correlation for the Stokes-flow drag force gives $F = 141$, which is much closer to that measured by Fand *et al.* The results of simulations presented in § 5 go some way toward explaining these observations, as well as identifying the approximate Reynolds numbers beyond which unsteady flow in random arrays of spheres persists at long times.

The lattice-Boltzmann method and our simulation methodology, including the generation of the sphere packings and details of the ensemble averaging, are explained in the accompanying paper (Hill *et al.* 2001). Nevertheless, to allow this paper to be reasonably self-contained, a brief description of the important parameters is given in the following section. Simulation results for moderate-Reynolds-number flows in face-centred, simple-cubic, and random arrays of spheres are presented in §§ 3, 4 and 5, respectively. These are followed by a summary of the results in § 6.

2. Simulation methodology

Details of the lattice-Boltzmann method and our computational methodology, beyond the slightly condensed description given here, may be found in §§ 2 and 3, respectively, of the accompanying paper (Hill *et al.* 2001). Note that all dimensional quantities, with the exception of the sphere radii and the size of the computational domains, are absorbed into the Reynolds number and dimensionless drag force, defined below. Lengths are measured in lattice units, with one lattice unit being the closest distance between the neighbouring nodes of the underlying cubic computational grid.

The porous media considered in this work are fixed periodic arrays of impermeable spheres with solid volume fractions

$$c = n(4/3)\pi a^3 = n_s(4/3)\pi(a/L)^3, \tag{2}$$

where n is the sphere number density, a is the sphere radius, and n_s is the number of spheres enclosed in the typically cubic computational domains whose volume is L^3. For simple cubic and face-centred cubic arrays of spheres, $n_s = 1$ and 4, respectively. For random arrays of spheres, n_s must be sufficiently large to minimize artifacts and statistical fluctuations coming from the finite size of the computational domain. In practice, n_s is chosen to be large enough to avoid periodic artifacts, and statistical uncertainty is reduced by ensemble averaging the results from n_c random sphere configurations.

Occasionally, only one or two random configurations were used to compute ensemble averages, particularly for computations requiring a large sphere radius and a large number of spheres in the computational domain. Under these conditions, the statistical error cannot be guaranteed to be sufficiently small. However, if the spheres in each random configuration are independent of one another, the *standard error* is expected to be inversely proportional to $(n_s n_c)^{1/2}$, and hence the statistical variation

coming from the small number of random configurations is expected to be small when n_s is large. The error bars used in presenting ensemble-averaged quantities indicate the standard error in the mean values.

The pressure and fluid velocity are governed by the incompressible Navier–Stokes equations, with the no-slip boundary condition at the sphere surfaces and periodic boundary conditions at the bounds of the computational domain. The fluid is typically accelerated from rest by a constant body force, which is equivalent to applying a constant average pressure gradient to the fluid.

The Reynolds number is defined as

$$Re = |\langle \boldsymbol{u} \rangle| a/\nu, \tag{3}$$

where ν is the fluid kinematic viscosity and $\langle \boldsymbol{u} \rangle$ is the spatially averaged velocity, which includes the volume occupied by the spheres.

At finite Reynolds numbers, the average velocity is not necessarily in the same direction as the average pressure gradient. In this work, flows are considered for which the applied body force is directed at an angle θ_p from the x-axis in the (x, y)-plane. For simple cubic and face-centred cubic arrays of spheres, the average velocity lies in the (x, y)-plane, but at an angle $\theta_u = \arctan(\langle u_y \rangle / \langle u_x \rangle)$ from the x-axis.

The non-dimensional drag force is defined as

$$F = |\langle \boldsymbol{f} \rangle| / (6\pi\mu a |\langle \boldsymbol{u} \rangle|), \tag{4}$$

where $\langle \boldsymbol{f} \rangle$ is the average drag force on the spheres. The denominator on the right-hand side of (4) is the Stokes drag force on a single sphere in an unbounded fluid, and hence positive deviations of F from unity indicate the contribution of hydrodynamic interactions (finite solid volume fraction) and fluid inertia (finite Reynolds number) to the magnitude of the average drag force.

At moderate Reynolds numbers, the spatial structure of the velocity field depends strongly on the solid volume fraction, the Reynolds number itself, and, for ordered arrays, the direction of the average pressure gradient relative to the axes of the arrays. In general, the dependence of the drag force on these parameters cannot be quantified by theoretical or heuristic scaling relationships. Nevertheless, it is helpful to consider the drag force as the sum of contributions from viscous and inertial stresses.

The viscous and inertial contributions are taken to be approximately proportional to the average velocity and the square of the average velocity, respectively, as might be expected based on simple scaling arguments. It follows that the viscous and inertial contributions to F are approximately independent of the Reynolds number and proportional to the Reynolds number, respectively. While this simplification is a good approximation for moderate-Reynolds-number flows in close-packed random arrays of spheres (Ergun 1952), nonlinear effects coupled with the ordered structure of simple cubic arrays – and to a lesser extent, face-centred cubic arrays – restrict its use to small ranges of the Reynolds number.

The magnitude of $\partial F / \partial Re$ at a given Reynolds number is used to indicate, at least qualitatively, the relative contribution of fluid inertia to the drag force. At the largest Reynolds numbers considered in this work, F often increases approximately linearly with the Reynolds number, and hence equations of the form

$$F = F_2(c) + F_3(c, \theta_u) Re \tag{5}$$

are fitted to simulation results. The magnitude of F_3 will be used to quantitatively compare simulations with different sphere configurations, solid volume fractions and, for ordered arrays, flow directions.

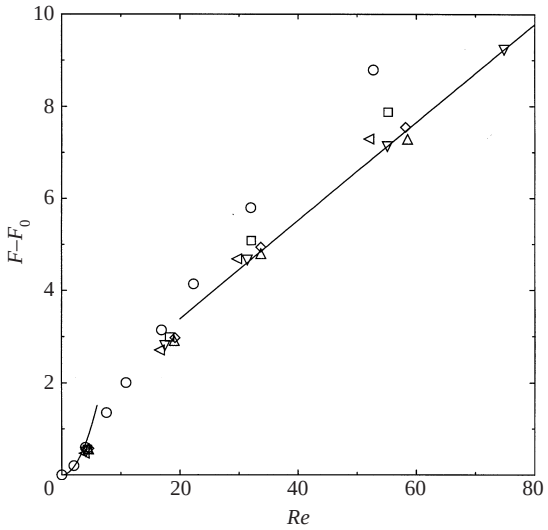

FIGURE 1. The inertial contribution to the non-dimensional drag force on the spheres in face-centred cubic arrays, with a nominal solid volume fraction of 0.3, as a function of the Reynolds number when the average pressure gradient is directed along the x-axis. The symbols are from lattice-Boltzmann simulations with $(a, c) = (6.8, 0.300)$ (○), (7.8, 0.294) (□), (8.8, 0.291) (◇), (10.8, 0.285) (△), (12.8, 0.318) (◁) and (16.8, 0.303) (▽), where a is in lattice units. The lines are the equations $F - F_0 = 0.042Re^2$ and $F - F_0 = 1.25 + 0.107Re$.

3. Face-centred cubic arrays

To determine how the grid resolution affects the dependence of F on the Reynolds number, simulations of finite-Reynolds-number flows in face-centred cubic arrays of spheres with sphere radii in the range 6.8–16.8 lattice units were performed. To reduce the computational cost, a single nominal solid volume fraction of 0.3 was chosen and the average pressure gradient was directed only along the x-axis. This solid volume fraction was chosen based on a compromise between the long time that it takes for the fluid velocity to reach steady state at small solid volume fractions and the larger number of lattice nodes required to accurately resolve velocity gradients at large solid volume fractions.

Figure 1 shows the inertial contribution to F, i.e. $F - F_0$, where F_0 is the non-dimensional Stokes-flow drag force, as a function of the Reynolds number for various sphere radii. This way of plotting the results helps to eliminate the effect of small differences in the solid volume fraction amongst the simulations with different sphere radii. Since $\partial F/\partial Re$ increases with the solid volume fraction, the effect of the slightly different solid volume fractions is most apparent at the largest Reynolds numbers.

Nevertheless, even at the largest Reynolds numbers, all the simulations, except, perhaps, those with a sphere radius of 6.8 or 7.8 lattice units, are in reasonable agreement with each other. The exceptional cases have an ostensibly larger drag force than obtained from the simulations with larger sphere radii, even when allowing for the different solid volume fractions.

With these relatively small sphere radii, the expected quadratic convergence of the lattice-Boltzmann method with increasing grid resolution is not observed. This is because a small change in the sphere radius changes the shapes of the spheres, giving rise to changes in the drag force that are comparable to those coming from the changing grid resolution. Nevertheless, such variations are small, and hence the

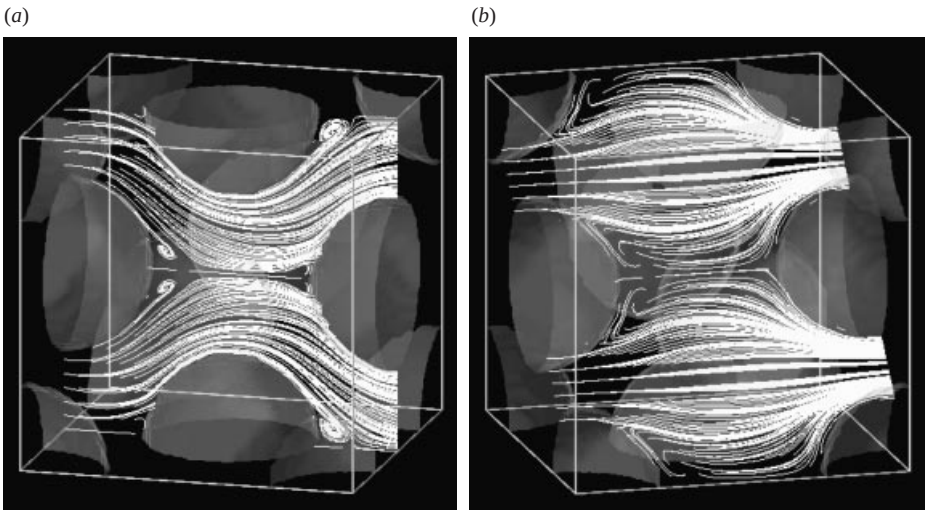

FIGURE 2. Streamlines, visualized on different planes, of a steady flow along the x-axis of a face-centred cubic array of spheres with $(c, a, Re, F) = (0.318, 12.8, 94.4, 26.4)$, where a is in lattice units. The unit normals of the planes on which the streamlines are shown are (a) $(0, 1, 0)$ and (b) $-(1/\sqrt{2})$ $(0, -1, 1)$.

accuracy of the simulations is reasonable over a wide range of sphere radii. For example, the maximum difference between $F - F_0$ amongst the simulations with sphere radii greater than 6.8 lattice units is approximately 10%, and the maximum difference in $\partial F/\partial Re$, at the largest Reynolds numbers where $F - F_0$ increases linearly with Re, is approximately 13%. For reference, the simulations with the largest sphere radius of 16.8 lattice units and a solid volume fraction of 0.303 give $F_3 = 0.107$ when $Re > 40$.

Figure 2 shows streamlines of a steady flow with a Reynolds number of 94.4 in a face-centred cubic array of spheres with a solid volume fraction of 0.318. The streamlines in the plane shown in (a) indicate the presence of recirculating flow attached to the rear of the spheres. While the recirculation in (a) is similar in appearance to the annular vortex attached to the rear of a single sphere in an unbounded fluid (Taneda 1956), (b), together with the fact that the flow is invariant to rotations of $\pi/2$ about the x-axis, shows that it is actually composed of four smaller recirculating flows.

In figure 2, and in those that follow, each streamline begins at a node of a uniform square grid lying in a plane whose unit normal is specified in the accompanying figure caption. The planes on which the streamlines are shown are chosen so there are no components of the fluid velocity normal to the plane. Therefore, the streamlines remain on the plane from which they originate, making them considerably easier to visualize. The spheres appear with a much courser surface than they actually have. This is simply due to the surfaces being identified in the visualizations by lattice nodes where the velocity is identically zero, whereas the boundary nodes that define the surfaces in the computations are actually halfway between lattice nodes.

Figure 3 shows the non-dimensional drag force on the spheres in face-centred cubic arrays as a function of the Reynolds number when the average pressure gradient is directed along the x-axis. Over this range of solid volume fractions, 0.48–0.698, $\partial F/\partial Re$ and F increase rapidly with the solid volume fraction. Fitting equations of

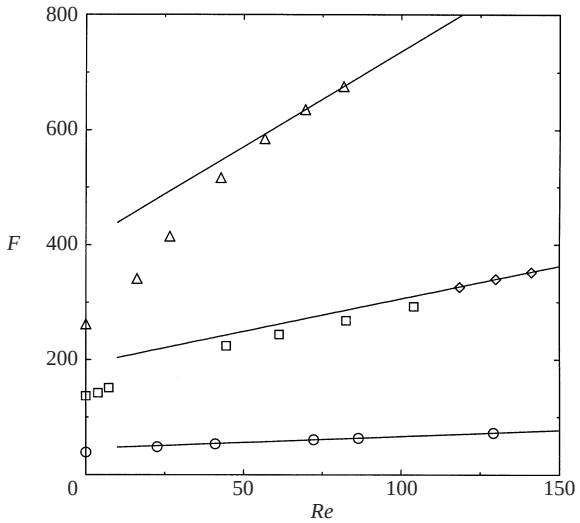

FIGURE 3. The non-dimensional drag force on the spheres in face-centred cubic arrays as a function of the Reynolds number for various solid volume fractions when the average pressure gradient is directed along the x-axis. The symbols are from lattice-Boltzmann simulations with $(a, c) = (20.8, 0.480)$ ($\bigcirc$), $(20.8, 0.633)$ ($\square$), $(30.8, 0.629)$ ($\diamond$) and $(20.8, 0.698)$ ($\triangle$), where a is in lattice units. The lines are equations of the form $F = F_2 + F_3 Re$, where $F_2 = 46.3$, 192 and 346, and $F_3 = 0.205$, 1.14 and 11.4, respectively.

the form given by (5) to the simulation results at the largest Reynolds numbers shows that each increase in the solid volume fraction by approximately 0.1 is accompanied by an approximately order of magnitude increase in F_3, whereas the corresponding increases in F_2 are considerably smaller. Note that $\partial F/\partial Re$ tends to decrease with increasing Reynolds number and the maximum values of $\partial F/\partial Re$ occur at Reynolds numbers of approximately 20.

Figure 4 shows the effect of changing the direction of the average pressure gradient relative to the axes of the arrays at three relatively large solid volume fractions. These simulations show that F, while it is not very sensitive to the direction of the average pressure gradient, increases when the flow is directed away from the x-axis. The increase of F with θ_p can be explained by considering the average fluid velocity in the regions halfway between the spheres in the flow direction. The fluid velocity there can be used to determine, qualitatively, how F changes with the direction of the flow. Since, from Bernoulli's equation, the difference between the pressures upstream and downstream of the spheres depends on the square of the velocity, the drag force will increase as the cross-sectional area through which the fluid flows decreases. In the following description, the cross-sectional area on the plane passing through the regions between the spheres in the flow direction will be referred to as the relative cross-sectional area, i.e. the cross-sectional area relative to that in the absence of the spheres.

For face-centred cubic arrays, a close examination of the geometry shows that the relative cross-sectional area when the flow is directed along the x-axis is $1 - \pi(a/L)^2$, whereas it is $1 - \sqrt{2}\pi(a/L)^2$ when $\theta_p = \pi/4$. The smaller cross-sectional area available when $\theta_p = \pi/4$ corresponds to a larger velocity between the spheres and, hence, a larger drag force, which is indeed what the simulations show. Similar considerations for simple cubic arrays of spheres give relative cross-sectional areas of 1 and $1 - \pi/\sqrt{2}(a/L)^2$ for $\theta_p = 0$ and $\pi/4$ respectively. Consequently, the drag force on the

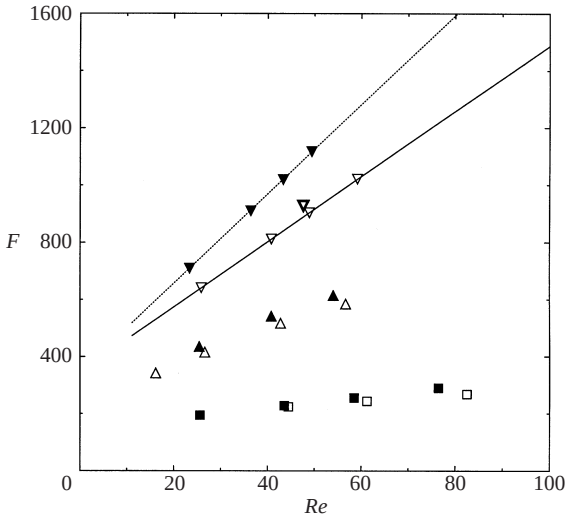

FIGURE 4. The non-dimensional drag force on the spheres in face-centred cubic arrays as a function of the Reynolds number for various solid volume fractions and directions of the average pressure gradient relative to the axes of the arrays. The symbols are from lattice-Boltzmann simulations with $(a, c) = (20.8, 0.633)$ (□), (20.8, 0.698) (△) and (31.8, 0.739) (▽), where a is in lattice units. The open (fine), open (bold) and filled symbols correspond to $\theta_p = 0$, $\pi/8$ and $\pi/4$, respectively, and the solid and dotted lines are the equations $F = 346 + 11.4Re$ and $F = 345 + 15.6Re$, respectively.

spheres in simple cubic arrays should also increase when the flow is directed away from the x-axis. In the next section, this will be shown to be the case. However, for simple cubic arrays, the increase in F with θ_p is much greater than for face-centred cubic arrays. This is because the simple cubic arrangement facilitates the development of recirculating flow in the gaps between the spheres in the flow direction.

At a solid volume fraction of approximately 0.63, which is close to the close-packed solid volume fraction for random arrays of spheres, F increases linearly with Re when the Reynolds number is greater than approximately 40. For example, the simulations with a solid volume fraction of 0.623 give $F_3 = 1.3$, whereas Ergun's correlation at this solid volume fraction gives $F_3 = 3.5$. Therefore, the drag force on the spheres in face-centred cubic arrays increases much more slowly with the Reynolds number than in random arrays with the same solid volume fraction, at least when the average pressure gradient is directed along the x-axis. Recall that the Stokes-flow drag forces on the spheres in random and ordered arrays are similar, and hence the sphere configuration affects the drag force considerably more at moderate Reynolds numbers.

Figures 5(*a*) and 5(*b*) show streamlines of steady flows in a face-centred cubic array of spheres when $\theta_p = 0$ and $\pi/4$, respectively. The solid volume fraction is 0.633, which is close to the solid volume fraction of close-packed random arrays of spheres. When the flow is directed along the x-axis, the velocity field has a similar structure to that observed by Wegner, Karabelas & Hanratty (1971) in experiments used to visualize the flow in a close-packed face-centred cubic array of spheres at a Reynolds number of 41. The most significant difference between the flow visualized in figure 5(*a*) and that for a close-packed array is that, because the spheres in figure 5 do not contact one another, there are no saddle points on the upstream sides of the spheres. Saddle points are points on the sphere surfaces where limiting streamlines converge and diverge. Wegner *et al.* (1971) also identified nodes and focal points,

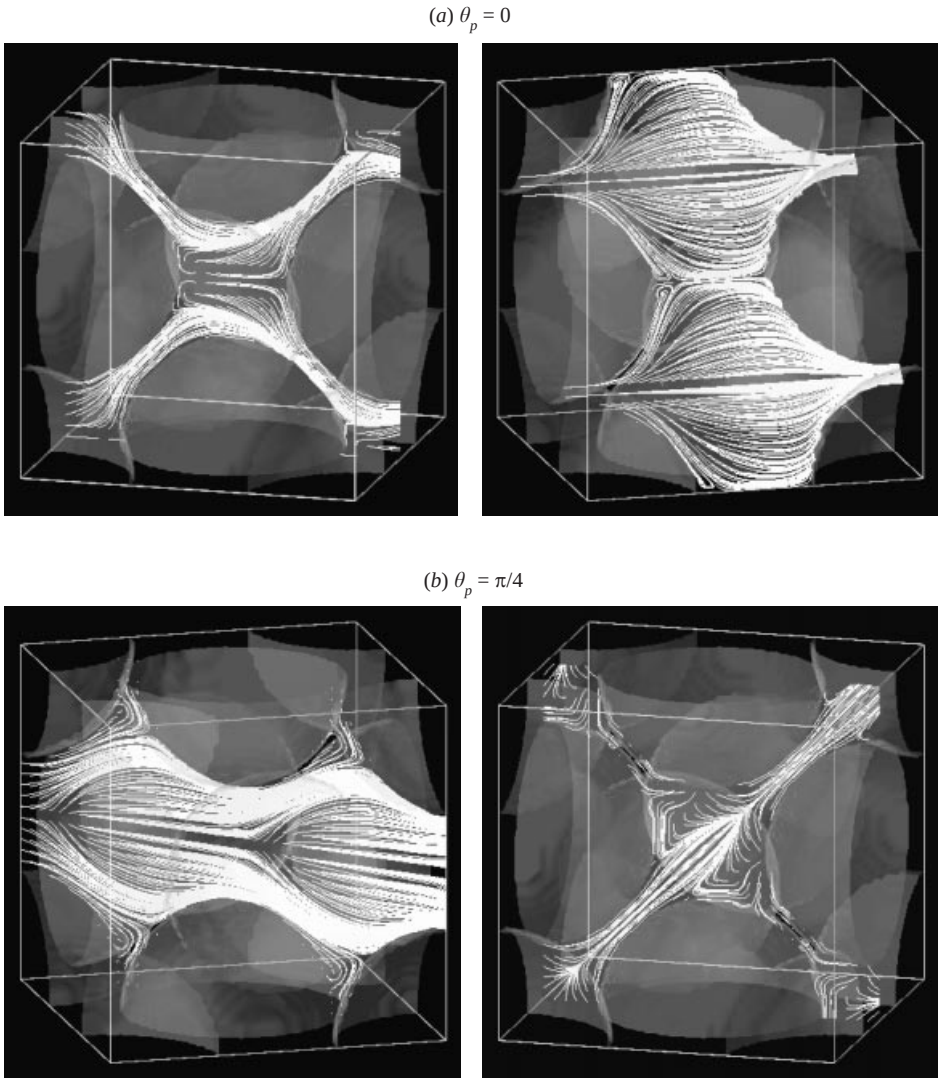

FIGURE 5. Streamlines, visualized on different planes, of steady flows in a face-centred cubic array of spheres with $(c, a) = (0.633, 20.8)$, where a is in lattice units: (*a*) $(\theta_p, Re, F) = (0, 61.3, 244)$; (*b*) $(\theta_p, Re, F) = (\pi/4, 58.5, 255)$. The unit normals of the planes on which the streamlines are shown are (*a*) $(0, 1, 0)$ (left), $(1/\sqrt{2})$ $(0, -1, 1)$ (right), and (*b*) $(1/\sqrt{2})$ $(1, 1, 0)$ (left), $(0, 0, 1)$ (right).

which distinguish other types of singular points in the pattern of limiting streamlines. Such details are difficult to observe from simulations, since the flow at the sphere surfaces is least resolved there. Nevertheless, they can be inferred, approximately, by observing the streamlines away from the surfaces.

Figure 6 shows the drag force on the spheres in a close-packed face-centred cubic array when the average pressure gradient is directed along the x-axis. The inertial contribution to F at this large solid volume fraction is proportional to Re^2 at Reynolds numbers up to approximately 2.5, and F increases linearly with Re at Reynolds numbers beyond approximately 10. The simulations give $F_3 = 11.0$, which is close to 10.4 given by Ergun's correlation at this solid volume fraction. Although

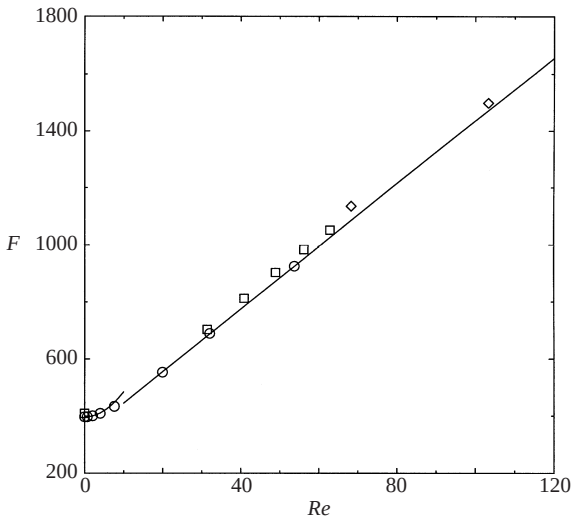

FIGURE 6. The non-dimensional drag force on the spheres in close-packed face-centred cubic arrays as a function of the Reynolds number when the average pressure gradient is directed along the x-axis. The symbols are from lattice-Boltzmann simulations with $(a, c) = (19.8, 0.741)$ (○), (31.8, 0.739) (□) and (48.8, 0.741) (◇), where a is in lattice units. The lines are the equations $F = 397 + 0.875Re^2$ and $F = 335 + 11.0Re$.

Ergun's correlation has not been tested experimentally at such a large solid volume fraction (this would require overlapping spheres or polydispersity), this suggests that the effects of fluid inertia on the drag force may be relatively independent of the sphere configuration when the solid volume fraction is sufficiently large. At Reynolds numbers greater than approximately 30, the spatially averaged velocity of the flows whose drag force is shown in figure 6 is actually unsteady.

4. Simple cubic arrays

These results cover a wide range of solid volume fractions, Reynolds numbers, and directions of the average pressure gradient relative to the axes of the arrays. For almost all of the simulations, the average velocity monotonically approached a steady state at long times. However, it is possible that if given sufficient time, slowly growing unstable modes could lead to unsteady flows. In cases where unsteady flow was detected at long times, the temporally and spatially averaged velocity was practically the same as that of the unstable steady flow existing before the onset of unsteady flow. Therefore, the dependence of the drag force on the Reynolds number, at least at these Reynolds numbers, does not depend very much on whether the flow is steady or not.

Since the effects of hydrodynamic interactions on the drag force at moderate Reynolds numbers can be most easily understood by considering moderate-Reynolds-number flow past a single sphere in an unbounded fluid, simulations with small solid volume fractions are considered first, followed by those with larger solid volume fractions.

4.1. *Dilute arrays*

Figure 7 shows the non-dimensional drag force on the spheres in a simple cubic array, with a solid volume fraction of 9.59×10^{-4} and a sphere radius of 0.734 lattice units,

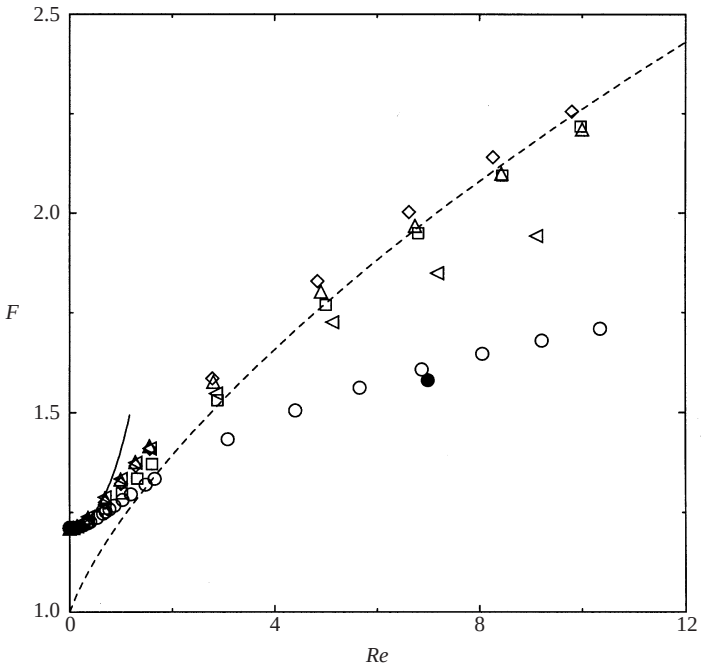

FIGURE 7. The non-dimensional drag force on the spheres in a simple cubic array as a function of the Reynolds number and the angle between the average pressure gradient and the x-axis in the (x, y)-plane. The symbols are from lattice-Boltzmann simulations with $(c, a) = (9.59 \times 10^{-4}, 0.734)$ (open) and $(1.03 \times 10^{-3}, 1.88)$ (filled), where a is in lattice units: $\theta_p = 0$ (○), $\pi/16$ (□), $\pi/8$ (◇), $3\pi/16$ (△) and $\pi/4$ (◁). The dashed line is for a single sphere in an unbounded fluid (Clift *et al.* 1978), and the solid line shows the $O(Re^2)$ inertial contribution to F when $\theta_p = 0$.

as a function of the Reynolds number. The various symbols correspond to different directions of the average pressure gradient relative to the axes of the array. The results of two simulations with a larger sphere radius of 1.88 lattice units give some indication of the effect of changing the grid resolution. At a Reynolds number of approximately 7, the resulting change in F is approximately 3%, and in the Stokes-flow limit the change is even less. The largest Reynolds number shown for each direction of the average pressure gradient indicates, approximately, the largest Reynolds number for which numerically stable solutions could be obtained. Simulations with a larger sphere radius would not only increase the accuracy of the results but would also increase the maximum Reynolds number that could be achieved. However, the long time that it takes for the average velocity to reach steady state at this solid volume fraction makes such computations prohibitively expensive. The time to reach steady state decreases with increasing Reynolds number, and hence the temporal evolution of the Stokes flows examined in the accompanying paper (Hill *et al.* 2001) gives a reliable upper bound on the time required for these flows to reach steady state.

The range of Reynolds numbers where the inertial contribution to F is proportional to Re^2 is very small. From the theory presented in the accompanying paper (Hill *et al.* 2001), this scaling is expected only when $Re_L \ll 1$, which at this solid volume fraction corresponds to $Re \ll 0.06$. Clearly, this prediction is in good agreement with the simulations. At much larger Reynolds numbers, the drag force is close to that on a single sphere in an unbounded fluid, particularly when θ_p is not too close to 0 or $\pi/4$. Under these conditions, the wakes behind the spheres have weak

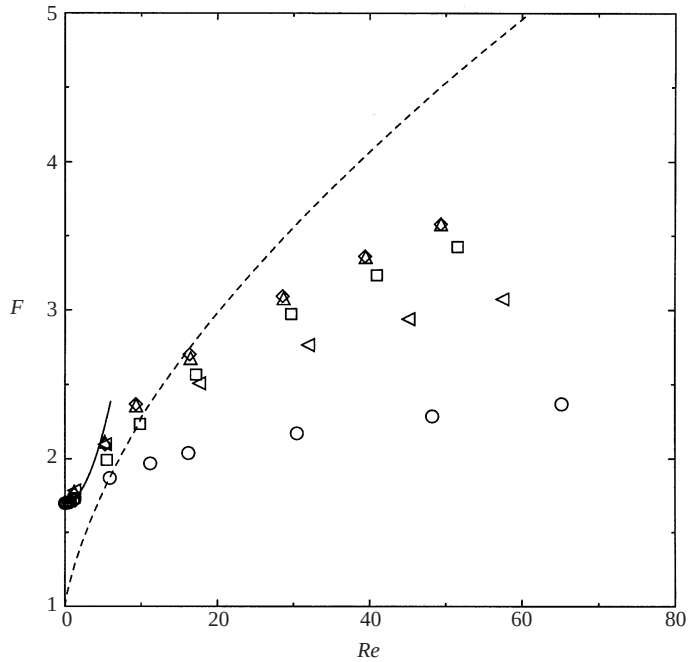

FIGURE 8. The non-dimensional drag force on the spheres in a simple cubic array as a function of the Reynolds number and the angle between the average pressure gradient and the x-axis in the (x, y)-plane. The symbols are from lattice-Boltzmann simulations with $(c, a) = (0.0141, 4.8)$, where a is in lattice units: $\theta_p = 0$ (○), $\pi/16$ (□), $\pi/8$ (◇), $3\pi/16$ (△) and $\pi/4$ (◁). The dashed line is for a single sphere in an unbounded fluid (Clift *et al.* 1978), and the solid line shows the $O(Re^2)$ inertial contribution to F when $\theta_p = 0$.

interactions with the spheres downstream, and hence fluid inertia decreases the strength of the hydrodynamic interactions. However, when θ_p is close to 0 or $\pi/4$, the momentum deficit in the wakes of the spheres interacts strongly with the spheres directly downstream. The relatively slowly moving fluid between the spheres decreases the difference between the pressures upstream and downstream of the spheres, and hence decreases the inertial contribution to the drag force. Note that this shielding effect does not necessarily require recirculating flow to span the gaps between the spheres – the Reynolds numbers of these simulations are actually smaller than the critical Reynolds number of approximately 10 beyond which streamlines separate from a single sphere in an unbounded fluid (Taneda 1956; Nakamura 1976; Johnson & Patel 1999). However, at larger solid volume fractions, recirculating flow does play a significant role in drag reduction.

Figure 8 shows the non-dimensional drag force on the spheres in a simple cubic array, with a solid volume fraction of 0.0141 and a sphere radius of 4.8 lattice units, as a function of the Reynolds number for various directions of the average pressure gradient. The larger sphere radius used for these simulations allows Reynolds numbers to be achieved where streamlines separate from the spheres and form recirculating flow. For all directions of the average pressure gradient, the drag force at Reynolds numbers greater than approximately 20 is smaller than that on a single sphere in an unbounded fluid. Furthermore, the average velocity is always in practically the same direction as the average pressure gradient.

Figures 9(*a*), 9(*b*) and 9(*c*) show streamlines and velocity vectors lying in the (x, y)-

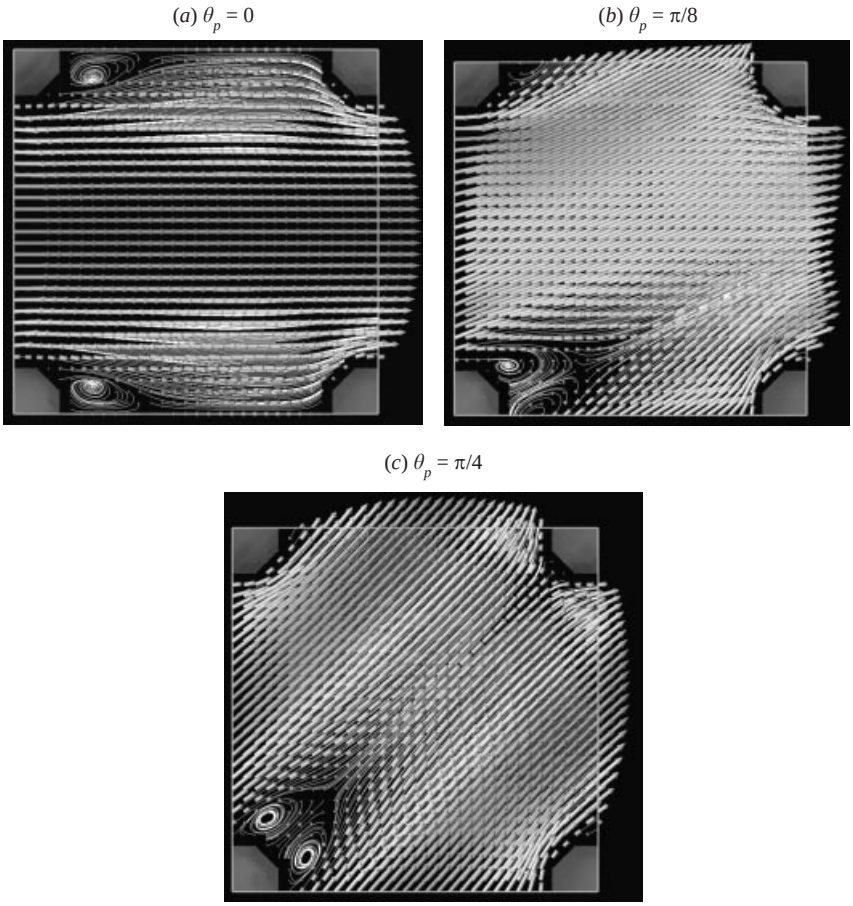

FIGURE 9. Streamlines and velocity vectors of steady finite-Reynolds-number flows in a simple cubic array of spheres with $(c, a) = (0.0141, 4.8)$, where a is in lattice units: (*a*) $(\theta_p, Re, F) = (0, 50.1, 2.30)$; (*b*) $(\theta_p, Re, F) = (\pi/8, 50.0, 3.60)$; (*c*) $(\theta_p, Re, F) = (\pi/4, 50.1, 3.00)$. The unit normal of the plane on which the streamlines are shown is $(0, 0, 1)$.

plane passing through the sphere centres when $\theta_p = 0$, $\pi/8$ and $\pi/4$, respectively. A large momentum deficit in the wakes of the spheres is apparent in (*a*) and (*c*). In (*b*), however, the momentum deficit diminishes more rapidly downstream, because of the large distance to the next sphere in the flow direction, and hence the drag force is much closer to that on a single sphere in an unbounded fluid. The length of the recirculating flow is approximately equal to that for a single sphere in an unbounded fluid at the same Reynolds number (Batchelor 1967) and is practically independent of the direction of the average velocity.

The foregoing observations, which distinguish moderate-Reynolds-number flows in dilute arrays from those with larger solid volume fractions, can be summarized as follows: (i) the recirculating flow in the wakes of the spheres is similar to that for flow past a single sphere in an unbounded fluid; (ii) the drag force at a fixed Reynolds number does not increase monotonically with θ_p; (iii) the drag force at large Reynolds numbers tends to be smaller than that on a single sphere in an unbounded fluid; and (iv) the average velocity is in practically the same direction as the average pressure gradient. These reflect that, while the fluid velocity close to the spheres

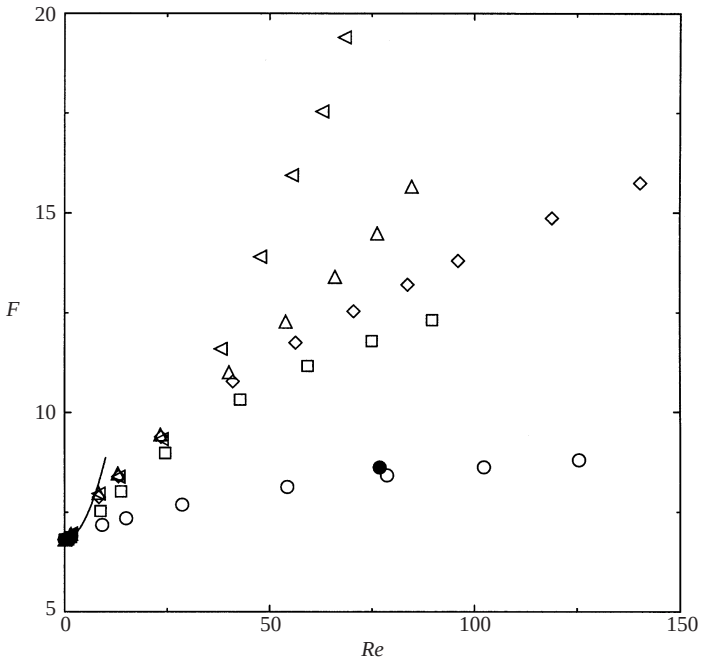

FIGURE 10. The non-dimensional drag force on the spheres in a simple cubic array as a function of the Reynolds number and the angle between the average pressure gradient and the x-axis in the (x, y)-plane. The symbols are from lattice-Boltzmann simulations with $(c, a) = (0.201, 17.8)$ (open) and (0.200, 9.8) (filled), where a is in lattice units: $\theta_p = 0$ (○), $\pi/16$ (□), $\pi/8$ (◇), $3\pi/16$ (△) and $\pi/4$ (◁). The solid line shows the $O(Re^2)$ inertial contribution to F when $\theta_p = 0$.

is similar to that for flow past a single sphere in an unbounded fluid, long-range hydrodynamic interactions decrease the drag force relative to that on a single sphere in an unbounded fluid. This effect is stronger at larger Reynolds numbers, because the momentum deficit in the wakes of the spheres extends further downstream.

4.2. *Moderate solid volume fractions*

At solid volume fractions of 0.0953 and 0.201, the dependence of the drag force on the Reynolds number and the direction of the average pressure gradient is qualitatively different to that shown above for dilute arrays. Note that results analogous to all those shown here for a solid volume fraction of 0.201, but for a solid volume fraction of 0.0953, can be found in the thesis of Hill (2001).

Figure 10 shows that F, at a given Reynolds number, increases monotonically with θ_p. At relatively large Reynolds numbers, F increases almost linearly with Re, particularly when the average pressure gradient is directed away from the x-axis. Furthermore, when the average pressure gradient is directed along the x-axis, F increases much more slowly with the Reynolds number.

Figure 11 shows the angle between the average velocity and the x-axis, at a solid volume fraction of 0.201, as a function of the Reynolds number. Note that the average velocity at a solid volume fraction of 0.0953 is in practically the same direction as the average pressure gradient. However, at a solid volume fraction of 0.201, the average velocity tends to move away from the x-axis when the Reynolds number is greater than approximately 10 and the average pressure gradient is not already directed along the x-axis. The average velocity moves back toward the x-axis as the Reynolds

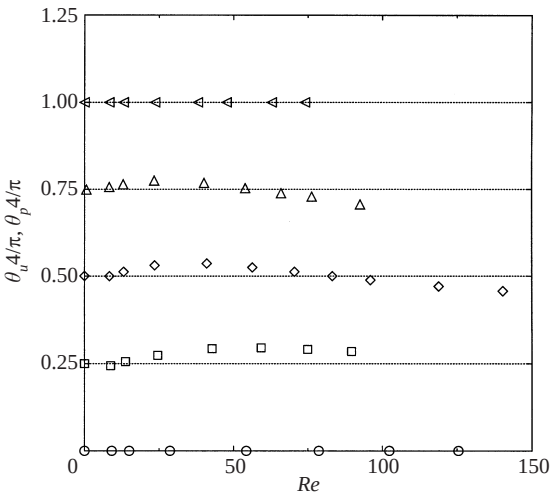

FIGURE 11. The angle between the average velocity and the x-axis in the (x, y)-plane as a function of the Reynolds number for the simulations whose non-dimensional drag force is shown in figure 10. The lines show the angle between the average pressure gradient and the x-axis in the (x, y)-plane.

number increases. At the largest Reynolds numbers shown, the average velocity is not necessarily in the same direction as the average pressure gradient, but tends to move toward the x-axis. Note that this is the direction in which the drag force is minimized for a given average velocity.

Figure 12 shows streamlines and velocity vectors of finite-Reynolds-number flows in a simple cubic array of sphere with a nominal solid volume fraction of 0.2. When the average pressure gradient is directed along the x-axis, recirculating flow spans the gaps between the spheres. The volume of recirculating fluid increases with the Reynolds number, which increases the fore-aft symmetry of the flow about the sphere centres. This decreases the difference between the pressures upstream and downstream of the spheres, and therefore decreases the inertial contribution to the drag force relative to the viscous contribution. Consequently, the drag force increases relatively slowly with the Reynolds number when the flow is directed along the x-axis, as shown in figure 10.

When the average pressure gradient is directed away from the x-axis, the momentum of the fluid flowing around the sides of the spheres prevents recirculating flow from contacting the spheres directly downstream. At the larger solid volume fraction (see figure 12), the fluid flowing through the gaps between the spheres undergoes a larger change in direction. This, together with the asymmetry of the flow about the sphere centres, increases the difference between the pressures upstream and downstream of the spheres, and therefore increases the inertial contribution to the drag force. Since, from Bernoulli's equation, pressure differences are approximately proportional to the square of the velocity, F increases approximately linearly with Re when the Reynolds number is large, as shown in figure 10.

4.3. *Dense arrays*

Figure 13 shows that, at a solid volume fraction of 0.408, there is a distinctive *decrease* in $\partial F/\partial Re$, which occurs at a Reynolds number of approximately 50. However, as shown in figure 10, at a solid volume fraction of 0.201, there is a distinctive *increase* in $\partial F/\partial Re$, which occurs at a Reynolds number of approximately 30. The decrease

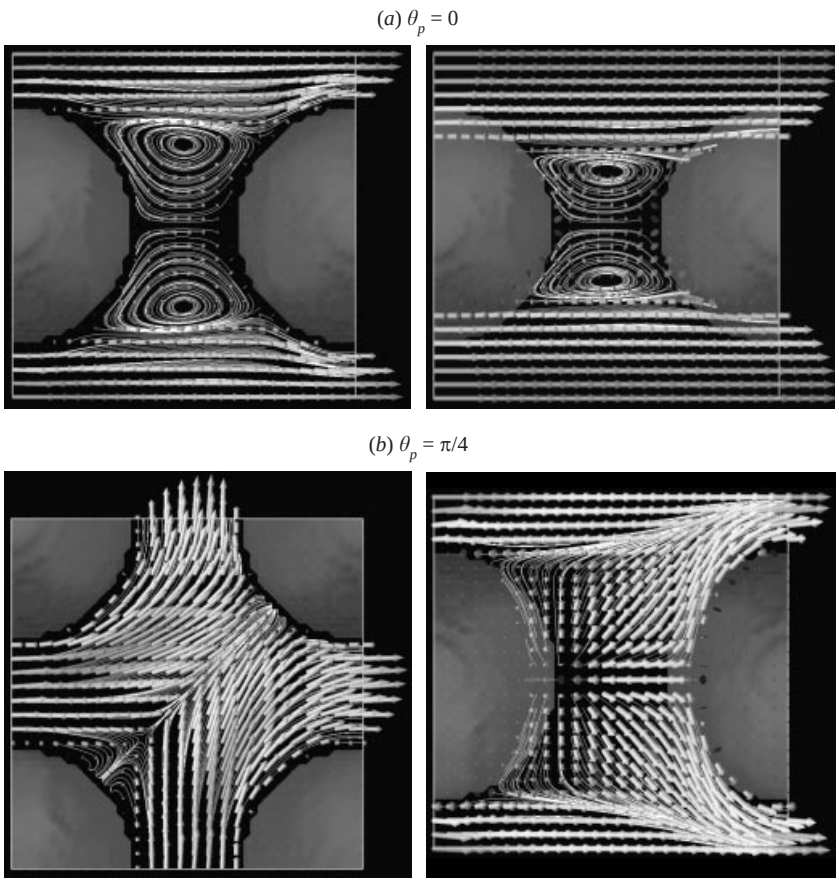

FIGURE 12. Streamlines and velocity vectors of steady flows in a simple cubic array of spheres with $(c, a) = (0.189, 17.8)$, where a is in lattice units: (*a*) $(\theta_p, Re, F) = (0, 52.5, 7.57)$; (*b*) $(\theta_p, Re, F) = (\pi/4, 52.7, 14.3)$. The unit normals of the planes on which the streamlines are shown are (*a*) (0, 1, 0) (left), $(1/\sqrt{2})$ (0, 1, 1) (right), and (*b*) (0, 0, 1) (left), $(1/\sqrt{2})$, $(1, -1, 0)$ (right).

in $\partial F/\partial Re$ at the larger solid volume fraction suggests that the relative contribution of viscous stresses to the drag force increases. By examining the velocity fields, this can be attributed to the smaller characteristic length scale of the more complex flow that exists at the larger solid volume fraction.

Figure 14 shows streamlines and velocity vectors of finite-Reynolds-number flows in a simple cubic array of spheres with a nominal solid volume fraction of 0.4 when $\theta_p = 0$ and $\pi/4$. When the average pressure gradient is directed along the x-axis, there are four large regions of recirculating flow between the spheres instead of the single region that was identified in figure 12(*a*) at a solid volume fraction of 0.189. When $\theta_p = \pi/4$, the fluid flowing through the smallest gaps between the spheres undergoes a rapid change in direction: the momentum of the fluid exiting the periodic cell, at least in this region of the flow, is practically perpendicular to its momentum on entry. Although this also occurs at a solid volume fraction of 0.189 (see figure 12*b*), there is a smaller length scale associated with the more complex flow at this solid volume fraction. Therefore, the smaller scales associated with the more complex flow field increase the viscous contribution to the drag force, and hence decrease $\partial F/\partial Re$.

Figure 15 shows the non-dimensional drag force on the spheres in a simple cubic

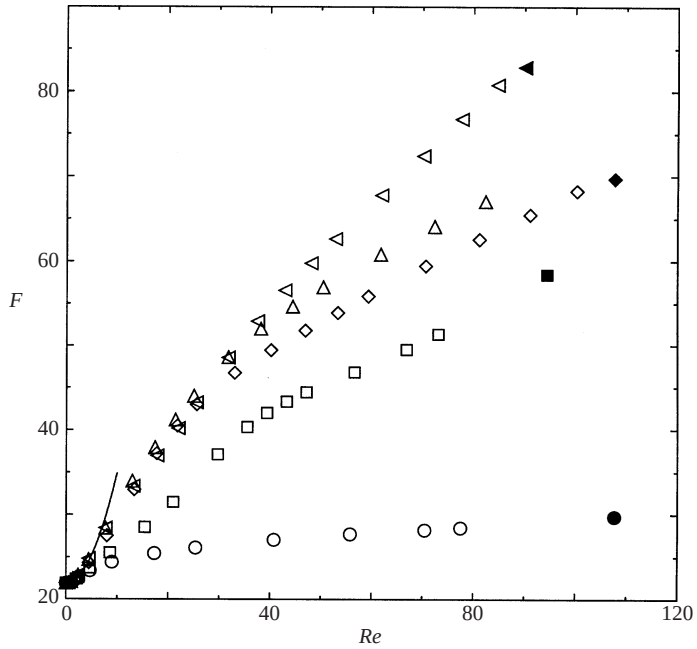

FIGURE 13. The non-dimensional drag force on the spheres in a simple cubic array as a function of the Reynolds number and the angle between the average pressure gradient and the x-axis in the (x, y)-plane. The symbols are from lattice-Boltzmann simulations with $(c, a) = (0.408, 18.8)$ (open) and (0.408, 36.8) (filled), where a is in lattice units: $\theta_p = 0$ (○), $\pi/16$ (□), $\pi/8$ (◇), $3\pi/16$ (△) and $\pi/4$ (◁). The solid line shows the $O(Re^2)$ inertial contribution to F when $\theta_p = 0$.

array, with a solid volume fraction of 0.514, as a function of the Reynolds number for various directions of the average pressure gradient. At a given Reynolds number, F increases monotonically with θ_p, but F changes relatively slowly with the flow direction when θ_p is in the range $\pi/8$–$\pi/4$. Furthermore, F increases approximately linearly with Re over a wide range of Reynolds numbers, which is typical of moderate-Reynolds-number flows in dense face-centred cubic and random arrays of spheres.

At this relatively large solid volume fraction, F_3 obtained from the simulations at the largest Reynolds numbers can be compared to that given by Ergun's correlation (1) for dense random arrays. Such a comparison is complicated by the fact that the drag force on the spheres in cubic arrays depends on the direction of the average pressure gradient relative to the axes of the arrays. From the simulations shown in figure 15, F_3 spans the range 0.12–2.6 as θ_p increases from 0 to $\pi/4$. However, averaging F_3 over the five directions of the average pressure gradient shown in figure 15 gives 1.7, which is close to 1.6 given by Ergun's correlation at this solid volume fraction. This rather crude estimate is based on only considering those directions where the average velocity lies in the (x, y)-plane. Nevertheless, it does show that the interactions between the spheres in dense random arrays may be dominated by the interaction of each sphere with its nearest neighbours. In the next section, where moderate-Reynolds-number flows in random arrays of spheres are examined, Ergun's correlation is compared to simulations over a wide range of solid volume fractions.

Figure 16 shows the angle between the average velocity and the x-axis as a function of the Reynolds number. At this solid volume fraction, there is a strong tendency for the average velocity to move toward the closer of the two directions corresponding

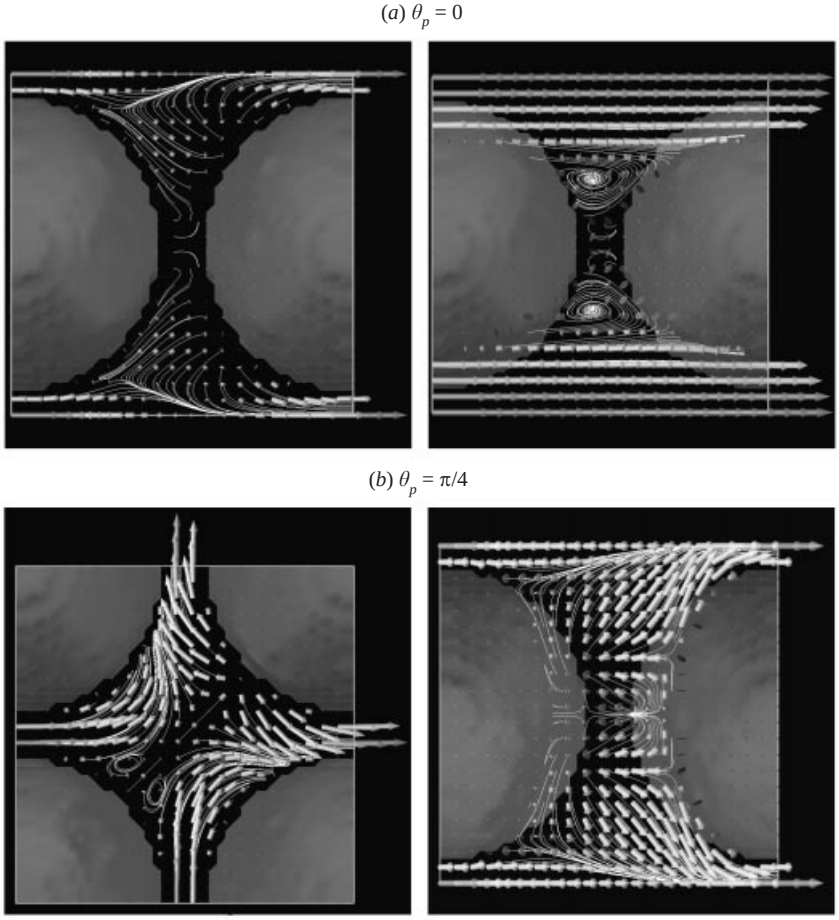

FIGURE 14. Streamlines and velocity vectors of steady flows in a simple cubic array of spheres with $(c, a) = (0.376, 18.8)$, where a is in lattice units: (*a*) $(\theta_p, Re, F) = (0, 68.8, 24.6)$; (*b*) $(\theta_p, Re, F) = (\pi/4, 60.0, 51.6)$. The unit normals of the planes on which the streamlines are shown are (*a*) $(0, 1, 0)$ (left), $(1/\sqrt{2})$ $(0, -1, 1)$ (right), and (*b*) (0, 0, 1) (left), $(1/\sqrt{2})$ $(1, -1, 0)$ (right).

to $\theta_u = 0$ and $\pi/4$. In these directions, the flows have symmetries that are otherwise broken when $0 < \theta_u < \pi/4$, and, unlike at smaller solid volume fractions, $\theta_u = \pi/4$ corresponds to a local minimum in the drag force at a given Reynolds number. Furthermore, these simulations show that $\theta_u = 0$ minimizes the drag force at any given Reynolds number and solid volume volume fraction.

When θ_p is close to $\pi/4$, at this solid volume fraction, the average velocity becomes unsteady at relatively small Reynolds numbers. Unsteady flows are indicated by the bold open symbols in figures 15 and 16. The unsteady behaviour, which developed after the flows first reached a practically steady state, shows that the apparently steady solutions were in fact unstable. In general, the transition to unsteady flow and the ensuing dynamics depend on the initial conditions and perturbations that may be applied to the unstable steady base state. The enhanced stability when the flow is directed along the x-axis is presumably related to the symmetries, the presence of straight-line trajectories, and the fact that the drag force is least there.

Figure 17 shows streamlines and velocity vectors of finite-Reynolds-number flows

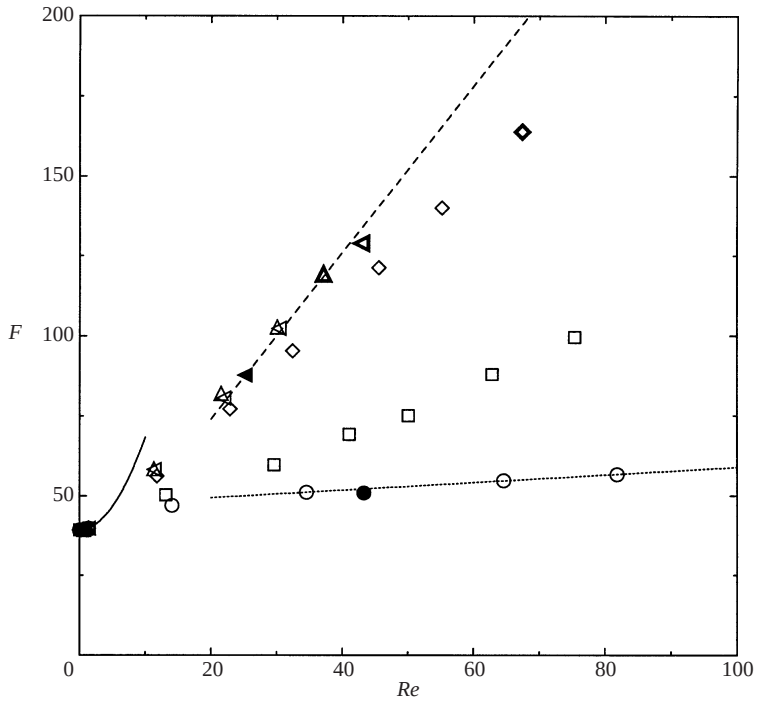

FIGURE 15. The non-dimensional drag force on the spheres in a close-packed simple cubic array as a function of the Reynolds number and the angle between the average pressure gradient and the x-axis in the (x, y)-plane. The symbols are from lattice-Boltzmann simulations with $(c, a) = (0.514, 32.8)$ (open) and (0.510, 22.8) (filled), where a is in lattice units: $\theta_p = 0$ (○), $\pi/16$ (□), $\pi/8$ (◇), $3\pi/16$ (△) and $\pi/4$ (◁). The solid line shows the $O(Re^2)$ inertial contribution to F when $\theta_p = 0$, and the dotted and dashed lines are the equations $F = 47.1 + 0.118Re$ and $F = 22.1 + 2.60Re$, respectively. The bold open symbols show time-averaged values for flows that were unsteady at long times.

in a close-packed simple cubic array of spheres when $\theta_p = 0$ and $\pi/4$. In contrast to the visualizations above with smaller solid volume fractions, there are large regions between the spheres where fluid moves slowly upstream. When the flow is directed along the x-axis, the straight-line trajectories referred to above are clearly those at the top and bottom of the computational domains shown in figure 17(*a*). Recall that the flow visualized in (*b*) represents, to a good approximation, the base state from which unsteady flow developed at only slightly larger Reynolds numbers. Similarly, the flow visualized in (*a*) represents, at least qualitatively, a base state that was found to be stable at considerably larger Reynolds numbers. This flow is characterized by an *inertial core* in which fluid moves with high velocity along the straight-line trajectories that can be seen at the top and bottom of the image to the right in figure 17(*a*).

5. Random arrays

5.1. *Drag force*

At large solid volume fractions, the close proximity of the spheres to their nearest neighbours screens the long-range hydrodynamic interactions that occur at smaller solid volume fractions. However, in a finite computational domain with periodic boundary conditions, long-range correlations in the fluid velocity may occur at finite Reynolds numbers if the fluid is able to flow directly through the computational do-

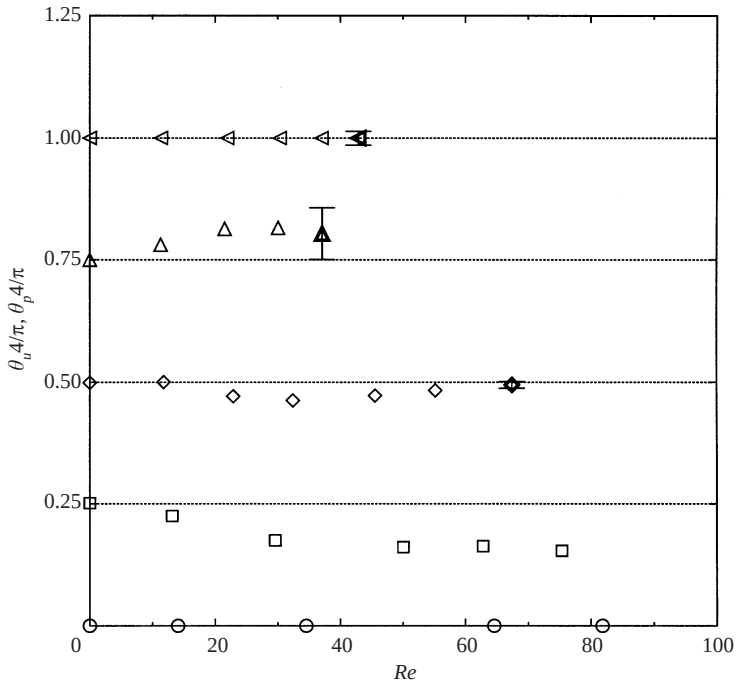

FIGURE 16. The angle between the average velocity and the x-axis in the (x, y)-plane as a function of the Reynolds number for the simulations whose non-dimensional drag force is shown in figure 15. The 'error' bars show the amplitude of the temporal fluctuations, and the lines show the angle between the average pressure gradient and the x-axis in the (x, y)-plane.

main. Such channels exist when either there are too few spheres in the computational domain or there is long-range order in a supposedly random sphere configuration. The relatively straight trajectories in such channels decreases the inertial contribution to the average pressure gradient and, hence, increases the velocity in the channels. The resulting increase in the average velocity and decrease in the average drag force have the combined effect of decreasing $\partial F/\partial Re$.

Simulations of finite-Reynolds-number flows in dense random arrays of spheres generated using the Monte-Carlo (MC) method (see Hill *et al.* 2001) with 16 and 32 spheres in the computational domain were compared to the results of simulations with sphere configurations generated using Zinchenko's method (Zinchenko 1994) with 64 spheres in the computational domain. In general, $\partial F/\partial Re$ from the simulations with configurations generated using the MC method were smaller than those obtained from the simulations with configurations generated using Zinchenko's method. This suggests that either there were too few spheres in the computational domains or that the supposedly random configurations had crystallized. Indeed, hard-sphere systems are known to undergo a transition from a disordered state to a face-centred cubic phase at a solid volume fraction of approximately 0.5 (Russel, Saville & Schowalter 1989). However, the time required for a disordered structure to reach its equilibrium state at large solid volume fractions can be very long, since the diffusivity at large solid volume fractions is small.

Nevertheless, to check for possible crystallization, the distribution of the angle between the vectors separating each sphere from its two nearest neighbours was calculated. This had distinct peaks at angles corresponding to $\pi/3$ and $2\pi/3$, suggesting

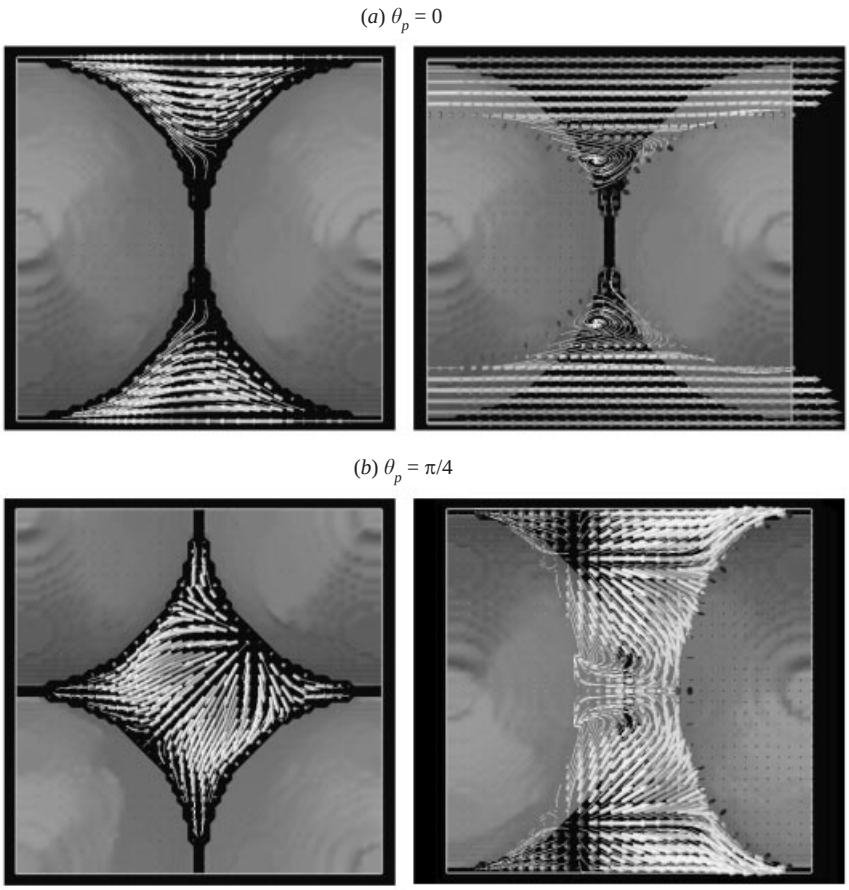

FIGURE 17. Streamlines and velocity vectors of steady flows in a close-packed simple cubic array of spheres with $(c, a) = (0.514, 32.8)$, where a is in lattice units: $(\theta_p, Re, F) = (0, 34.7, 51.0)$; (*b*) $(\theta_p, Re, F) = (\pi/4, 25.0, 88.3)$. The unit normals of the planes on which the streamlines are shown are (*a*) $(0, 1, 0)$ (left), $(1/\sqrt{2})$ $(0, -1, 1)$ (right), and (*b*) $(0, 0, 1)$ (left), $(1/\sqrt{2})$ $(1, -1, 0)$ (right).

that the arrays may have crystallized. Since it was impractical to generate larger close-packed arrays using the MC algorithm, the configurations generated using Zinchenko's method with 64 spheres were subsequently used for simulations with solid volume fractions greater than approximately 0.5. The solid volume fraction of the configurations generated using Zinchenko's method is as close as possible to the close-packed limit of random arrays of spheres. Therefore, to achieve smaller solid volume fractions, the sphere radius was first decreased and then MC steps were applied to allow the configurations to 'relax'. The distributions of the angle between each sphere and its two nearest neighbours for these arrays were more uniform, suggesting that the configurations were more 'random' than those obtained using the MC method alone.

Figures 18–24 show the non-dimensional drag force on the spheres in random arrays with nominal solid volume fractions of $0.1i\,(i = 1 \ldots 6)$. At Reynolds numbers greater than approximately 40, F increases approximately linearly with Re, as suggested by Ergun's correlation. In all the figures showing F as a function of Re, the results of simulations with a relatively small sphere radius and a relatively small number of

c	a	L_x/L_y	n_s	n_c	F_0	F_1	F_2	F_3
0.0953	6.8	2	128	1	2.88	0.100	3.87	0.111
0.0953	6.8	3	192	1	—	—	3.52	0.103
0.0960	6.8	1	32	5	2.87	0.0867	3.38	0.101
0.100	4.8	1	16	5	—	—	3.28	0.118
0.192	8.8	1	16	4	4.98	0.0915	5.35	0.147
0.201	8.8	1	16	5	5.74	—	6.10	0.176
0.224	9.8	2	128	1	6.61	0.125	7.80	0.204
0.290	8.8	1	16	5	9.35	0.152	10.5	0.257
0.300	10.8	2	128	1	10.5	0.148	11.9	0.320
0.408	16.8	1	16	5	—	—	24.9	0.528
0.408	16.8	1	128	1	20.5	0.195	23.4	0.488
0.413	8.8	1	16	5	21.5	0.213	22.6	0.581
0.413	8.8	1	128	1	—	—	21.7	0.545
0.472[1]	19.8	1	64	1	34.2	0.229	37.3	0.690
0.474	16.8	1	60	1	33.7	0.207	34.7	0.841
0.500	16.8	1	16	5	42.0	0.352	45.7	0.950
0.547[1]	20.8	1	64	1	60.1	0.379	65.9	1.36
0.555	17.8	1	16	2	63.1	0.255	63.0	1.21
0.568	16.8	1	60	1	73.2	0.345	75.1	1.66
0.589[1]	20.8	1	64	1	83.9	0.598	87.1	2.16
0.620[1]	23.8	1	64	1	109	0.792	106	3.27
0.641	20.8	1	16	2	141	0.431	134	3.35

TABLE 1. The parameters used for selected lattice-Boltzmann simulations of finite-Reynolds-number flows in random arrays of spheres. The coefficients F_2 and F_3 in equations of the form $F = F_2 + F_3 Re$ were obtained from the simulations with the largest Reynolds numbers at each solid volume fraction. [1]The sphere configurations for these simulations were initialized with configurations generated using the method of Zinchenko (1994).

spheres in the computational domain are shown. These clearly show the qualitative dependence of F on Re. However, to validate the accuracy of these simulations, and to obtain more accurate estimates of F_3 at the largest Reynolds numbers, the results of a smaller number of simulations are shown, which have a larger sphere radius and a larger number of spheres in the computational domain. Note that, because the solid volume fractions could not be matched exactly, part of the difference between the results comes from statistical fluctuations and the various grid resolutions, system sizes, and solid volume fractions. The error bars show the standard error (see Hill *et al.* 2001) in the ensemble-averaged F and Re. Simulation parameters and the values of F_2 and F_3 obtained at Reynolds numbers where F increases linearly with Re are listed in table 1. Also shown are the coefficients F_0 and F_1 in equations fitted to the simulation results, at small Reynolds numbers, where the non-dimensional drag force takes the form (Hill *et al.* 2001).

$$F = F_0 + F_1 Re^2. \tag{6}$$

Note that simulations were also performed with a computational domain whose length in the x-direction, L_x, was two or three times longer than in the y- and z-directions ($L_y = L_z$). The nominal solid volume fractions of these simulations were chosen to be 0.1, 0.2 and 0.3, since the wakes behind the spheres at relatively

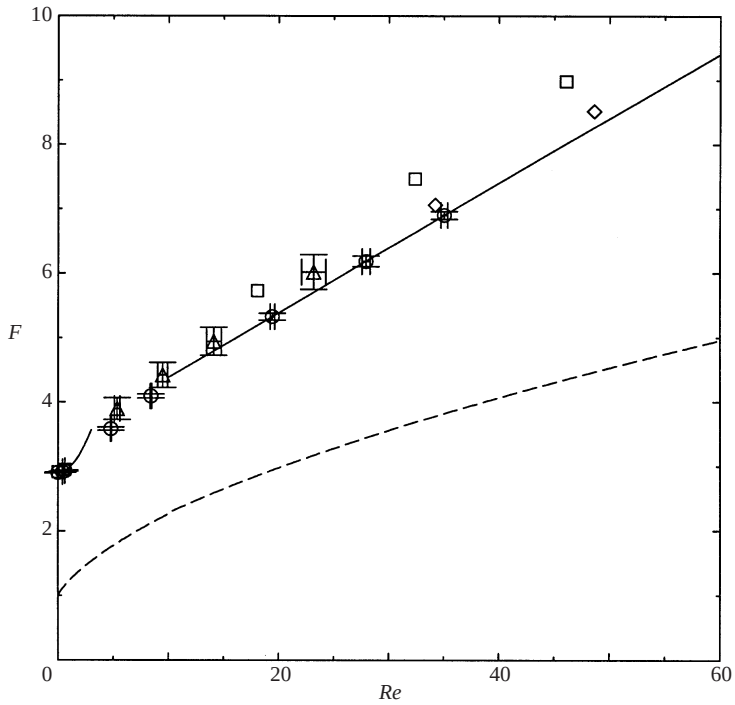

FIGURE 18. The non-dimensional drag force on the spheres in random arrays with a nominal solid volume fraction of 0.1 as a function of the Reynolds number. The symbols are from lattice-Boltzmann simulations with $(c, a, L_x/L_y, n_s, n_c) = (0.0960, 6.8, 1, 32, 2)$ (○), $(0.0953, 6.8, 2, 128, 1)$ (□), (0.0953, 6.8, 3, 192, 1) (◇) and (0.100, 4.8, 1, 16, 5) (△), where a is in lattice units. The dashed line is the empirical equation (Hill *et al.* 2001, equation (46)) for a single sphere in an unbounded fluid (Clift *et al.* 1978), and the solid lines are quadratic and linear fits to the simulation results identified with circles. The error bars show the standard errors in the ensemble-averaged F and Re.

small solid volume fractions are most likely to interact with their periodic images downstream. However, as shown in figures 18–20, no significant, systematic change in the dependence of F on the Reynolds number with the size of the computational domain can be detected. This confirms that the simulations give a good approximation of the drag force on the spheres in infinite arrays.

In general, the range of Reynolds numbers where the inertial contribution to F is proportional to Re^2 increases with the solid volume fraction. The coefficient of Re^2 was examined in the accompanying paper (Hill *et al.* 2001) at solid volume fractions up to the close-packed limit. Recall that Kaneda's theory for dilute random arrays of spheres is valid when the Reynolds number based on the Brinkman screening length is very small. Since the Brinkman screening length decreases with increasing solid volume fraction, the Reynolds numbers where the Re^2 scaling occurs is expected to increase with the solid volume fraction. This is indeed the case, as shown in figure 22, for example, where at a solid volume fraction of 0.413 the inertial contribution to F is proportional to Re^2 at Reynolds numbers up to approximately 1.2. At very small solid volume fractions, Kaneda's theory shows that Re^2 scaling occurs when $Re \ll O(c^{1/2}) \ll 1$. Although it is difficult to see in figure 18, the inertial contribution to F at a solid volume fraction of 0.0960 is proportional to Re^2 at Reynolds numbers up to approximately 0.75. At the close-packed limit, Re^2 scaling was shown in the

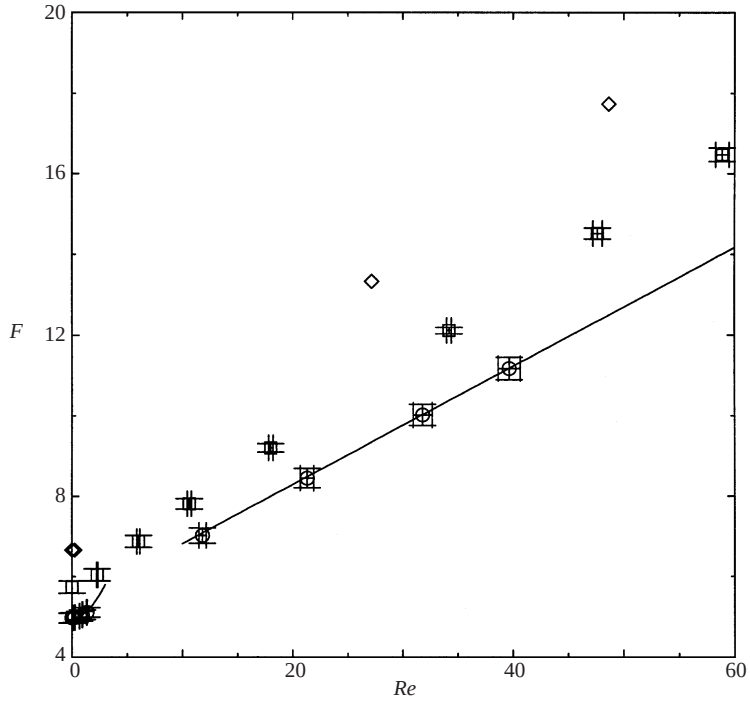

FIGURE 19. As figure 18 but with a nominal solid volume fraction of 0.2 and $(c, a, L_x/L_y, n_s, n_c) = (0.192, 8.8, 1, 16, 4)$ (○), (0.201, 8.8, 1, 16, 5) (□) and (0.224, 9.8, 2, 128, 1) (◇).

accompanying paper to occur at Reynolds numbers up to approximately 2.6, which is consistent with the qualitative behaviour identified here.

The simulation results identified with circles in figure 18 were obtained from only two random configurations, since the long time that it takes for the velocity to reach a steady state at this relatively small solid volume fraction makes these simulations particularly expensive. However, five random configurations were used to calculate F at the two largest Reynolds numbers, giving $F_3 = 0.104$ with a standard error of approximately 3%. The standard errors in the Reynolds numbers obtained from these simulations were approximately 1.2%.

5.2. *Comparison of simulations with the Ergun correlation*

Ergun's correlation is compared to the simulations identified with circles in figures 20–24, at nominal solid volume fractions in the range 0.3–0.6. In all cases, Ergun's correlation under-predicts the drag force given by the simulations at small Reynolds numbers and over-predicts the drag force at larger Reynolds numbers. This is clearly due to F_3 from Ergun's correlation being too large, particularly at the smaller solid volume fractions, and F_2 being too small. Nevertheless, as shown in figure 24, there is considerably better agreement at nominal solid volume fractions of 0.6. This is, perhaps, not surprising, since in experiments it is only when the particles are closely packed that their configuration might be considered to approximate a 'random' hard-sphere distribution. Otherwise, cohesive forces and ordering are required to maintain a rigid structure whose solid volume fraction is less than the close-packed limit.

Before we consider how the particle configuration might affect the drag force, note that Ergun compared his correlation to experiments by plotting $\log_{10}(18F(1-c)^3/c)$

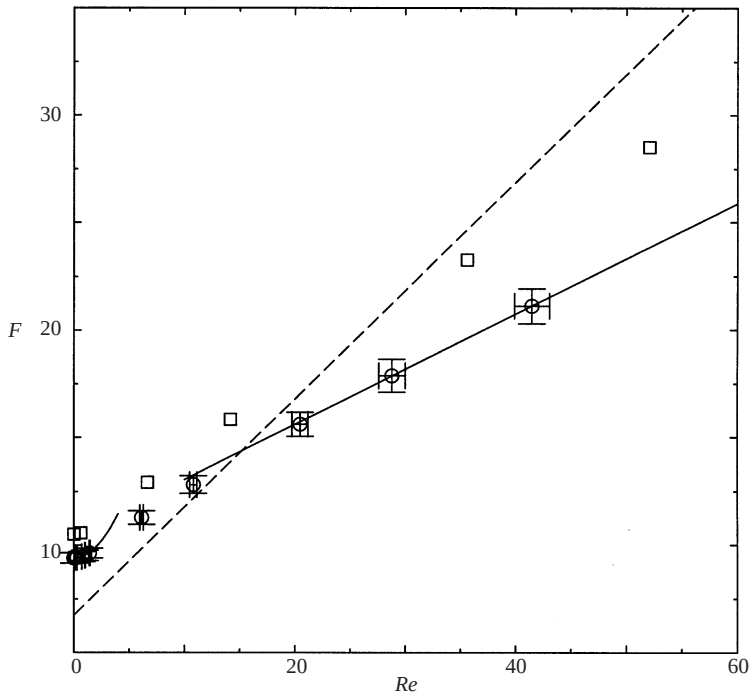

FIGURE 20. As figure 18 but with a nominal solid volume fraction of 0.3 and $(c, a, L_x/L_y, n_s, n_c) = (0.290, 8.8, 1, 16, 5)$ (○) and $(0.300, 10.8, 2, 128, 1)$ (□). The dashed line is from Ergun's correlation (1) (Ergun 1952) with $c = 0.290$.

as a function of $\log_{10}(2Re/c)$ without identifying the solid volume fractions of the individual experimental results. The experiments were performed using packed beds of coke particles that were sieved to obtain relatively narrow size distributions. Solid volume fractions in the range 0.46–0.56 were achieved by compressing the packings while they were maintained in a fluidized state. The Reynolds numbers that were achieved can be estimated to be in the range 1.6–60. Therefore, the scatter due to experimental error cannot be distinguished from the variations coming from the various solid volume fractions and particle shapes. Despite this scatter, however, it is reasonable to conclude that Ergun's correlation tends to over-predict the ordinate at large values of $2Re/c$, which suggests that it might also tend to over-predict F at large Reynolds numbers and, possibly, at small solid volume fractions too.

Another explanation for the difference between Ergun's correlation and our simulation results is due to the fact that the packings with solid volume fractions in the range 0.46–56 reported by Ergun would have required a network of touching particles to coexist with a network of void spaces and empty channels. The backbone of such a particle network might give rise to a larger inertial contribution to the drag force, since the wakes behind the spheres would more often have to extend further downstream before they are obstructed by other particles in the network. At small Reynolds numbers, when the largest contribution to the drag force comes from viscous stresses, the drag force on such a network would be smaller, since the more open structure would have a larger characteristic pore size and, hence, smaller viscous stresses acting on the particles. These are the trends identified from the comparison of Ergun's correlation with the simulation results shown in figures 20–24.

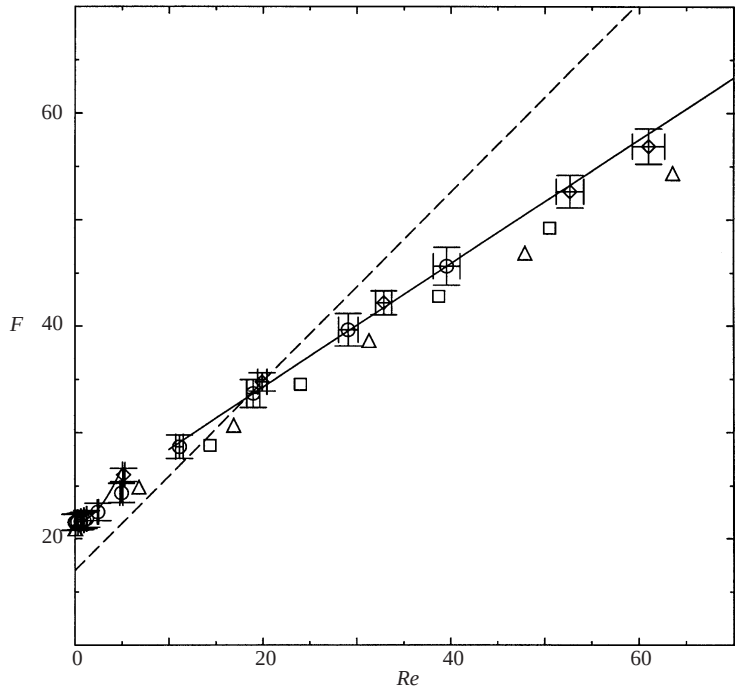

FIGURE 21. As figure 18 but with a nominal solid volume fraction of 0.4 and $(c, a, L_x/L_y, n_s, n_c) = (0.413, 8.8, 1, 16, 5)$ (○), (0.413, 8.8, 1, 128, 1) (□), (0.408, 16.8, 1, 16, 5) (◇) and (0.413, 16.8, 1, 128, 1) (△). The dashed line is from Ergun's correlation (1) (Ergun 1952) with $c = 0.413$.

Figure 25 compares F_3 obtained from the simulations at the largest Reynolds numbers where F increases linearly with Re to F_3 given by Ergun's correlation (dashed line). While there is good agreement at solid volume fractions greater than approximately 0.6, Ergun's correlation predicts much larger values of F_3 and, hence, a larger drag force at smaller solid volume fractions. The simulation results are given to a good approximation by the fit

$$F_3 = 0.0673 + 0.212c + 0.0232/(1 - c)^5, \tag{7}$$

which is shown as the solid line. When extrapolated to a solid volume fraction of 0.64, (7) is in good agreement with the experiments of Fant *et al.* (1987), which were performed with spherical glass spheres with a relatively narrow size distribution. Good agreement is also found between our lattice-Boltzmann simulations and those of Maier *et al.* (1998) for flow in a cylindrical packed bed of spheres with a solid volume fraction of 0.568.

It is important to note that F_3 was obtained from simulations at the largest Reynolds numbers where F increases linearly with Re. Therefore, it does not account for the transition region that exists at smaller Reynolds numbers where $\partial F/\partial Re$ may be considerably larger than F_3. Fitting splines to F versus Re from the simulations and then plotting $\partial F/\partial Re$ versus Re showed that $\partial F/\partial Re$ reaches a maximum at Reynolds numbers in the range 10–20 before decaying toward F_3 at larger Reynolds numbers. The maximum of $\partial F/\partial Re$ is 10–60% larger than F_3, with the largest differences occurring at the smallest solid volume fractions. Consequently, F_3 given by (7) is a better approximation of $\partial F/\partial Re$ over a wider range of Reynolds numbers when the

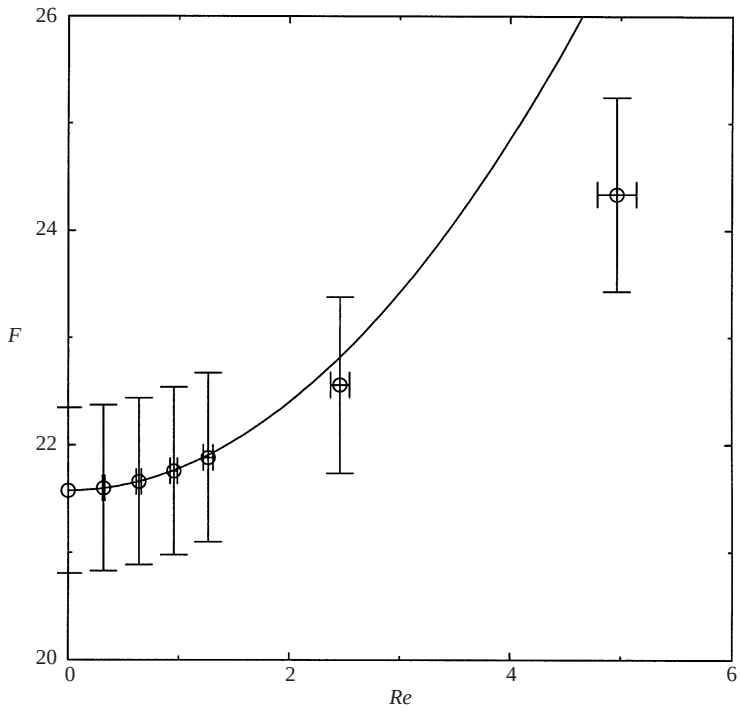

FIGURE 22. The simulations identified with circles in figure 21, but with the axes scaled to detail the limit $Re \to 0$.

solid volume fraction is relatively large. Unfortunately, the statistical fluctuations in the results prohibits a more quantitative analysis of the dependence of $\partial F/\partial Re$ on the Reynolds number and the solid volume fraction.

The vertical line in figure 25 shows the range of F_3 that comes from changing the direction of the average pressure gradient in a close-packed simple cubic array of spheres. The diamond shows F_3 for flow along the $(1, 0, 0)$ axis of a face-centred cubic array of spheres with a solid volume fraction corresponding to the close-packed limit of random arrays of spheres. Recall that the drag force on the spheres in face-centred cubic arrays with large solid volume fractions does not depend very much on the direction of the average pressure gradient (see figure 4). The comparisons show that, at finite Reynolds numbers, the long-range order of simple cubic arrays of spheres may either increase or decrease F_3 relative to that for random arrays. Clearly, the sphere configuration plays an increasingly important role in determining the drag force at moderate Reynolds numbers.

5.3. *Flow topology, velocity variance, and hydrodynamic dispersion*

Figure 26 compares the velocity field of a flow with a Reynolds number of 26.9 to that of a Stokes flow with exactly the same geometry. The solid volume fraction of the array is 0.0960. Note that the length of the recirculating flow attached to the rear of a single sphere in an unbounded fluid at a Reynolds number of 30 is approximately $1.2a$ (Batchelor 1967). However, even at this relatively small solid volume fraction, recirculating flow in the wakes of the spheres cannot be seen, except, perhaps, between a small number of spheres that are very close to each other. This suggests that the velocity disturbances created by the randomly positioned spheres

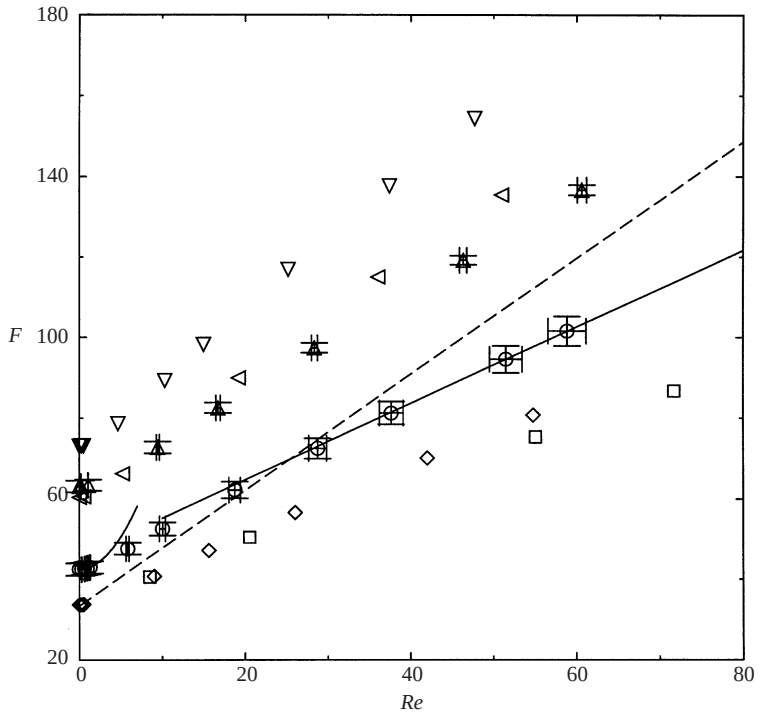

FIGURE 23. As figure 18 but with a nominal solid volume fraction of 0.5 and $(c, a, L_x/L_y, n_s, n_c) = (0.500, 16.8, 1, 16, 5)$ (○), (0.472, 19.8, 1, 64, 1) (□) and (0.474, 16.8, 1, 60, 1) (◇). Also shown are results with $(c, a, L_x/L_y, n_s, n_c) = (0.555, 17.8, 1, 16, 2)$ (△), (0.547, 20.8, 1, 64, 1) (◁) and (0.568, 16.8, 1, 60, 1) (▽). The dashed line is from Ergun's correlation (1) (Ergun 1952) with $c = 0.500$.

prohibits recirculating flow from developing in their wakes, at least at this Reynolds number and solid volume fraction.

The disturbances to the transverse components of the fluid velocity, which can be can be seen in figure 26, are smaller at a finite Reynolds number. The velocity variance of the Stokes flow is $0.450|\langle \boldsymbol{u} \rangle|^2$, which is close to the value of $0.420|\langle \boldsymbol{u} \rangle|^2$ at a Reynolds number of 26.9. However, as expected from the visual comparison of the flows, the transverse velocity variances of the flows are very different. For the Stokes flow, $(\langle u_y' \rangle^2 + \langle u_z' \rangle^2)/2 = 0.195|\langle \boldsymbol{u} \rangle|^2$, whereas at a Reynolds number of 26.9, $(\langle u_y' \rangle^2 + \langle u_z' \rangle^2)/2 = 0.0719|\langle \boldsymbol{u} \rangle|^2$, which is approximately 63% smaller. Therefore, the effect of moderate Reynolds numbers on hydrodynamic dispersion would be to decrease the rate at which the transverse component of the effective hydrodynamic diffusivity increases with the Péclet number. Furthermore, a significant hold-up contribution to the longitudinal component of the effective diffusivity is unlikely, since there are very few regions of fluid bounded by closed streamlines. Recall that the spheres in simple cubic arrays with nominal solid volume fractions of 0.1 and 0.2 had a considerable volume of recirculating fluid in their wakes (see figure 12), which would give rise to hold-up dispersion.

At larger solid volume fractions, more of the fluid is directly influenced by the presence of the spheres. The close proximity of the fluid to the sphere surfaces increases the contribution of the transverse components of the velocity disturbances to the velocity variance. Furthermore, since most of the velocity disturbances at large

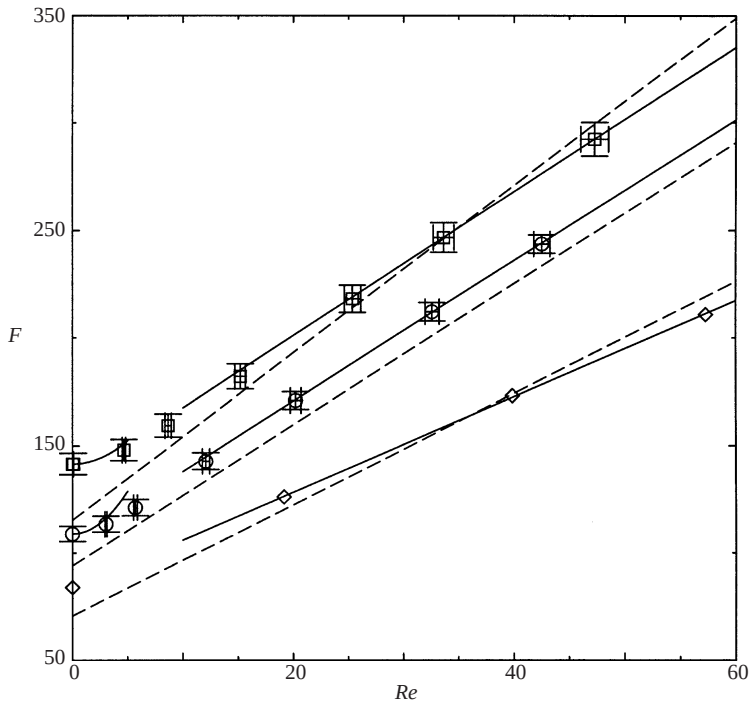

FIGURE 24. As figure 18 but with a nominal solid volume fraction of 0.6 and $(c, a, L_x/L_y, n_s, n_c) = (0.620, 23.8, 1, 64, 3)$ (○), (0.641, 20.8, 1, 16, 2) (□) and (0.589, 20.8, 1, 64, 1) (◇). The dashed lines are from Ergun's correlation (1) (Ergun 1952).

solid volume fractions come from fluid having to move through the tortuous paths between the spheres, the velocity variance, when scaled with the square of the average velocity, does not depend very much on the Reynolds number. At a solid volume fraction of 0.588, for example, figure 27 compares the velocity field of a flow with a Reynolds number of 23.3 to that of a Stokes flow.

The velocity variance of the Stokes flow is $5.38|\langle \boldsymbol{u} \rangle|^2$, which is close to $5.58|\langle \boldsymbol{u} \rangle|^2$ at a Reynolds number of 23.3. The small increase in the scaled velocity variance comes from the larger velocity gradients and the development of a small number of regions with recirculating flow. However, in contrast to the flows discussed above with a solid volume fraction of 0.0960, the transverse velocity variance of these flows is very similar. For the Stokes flow, $(\langle u_y' \rangle^2 + \langle u_z' \rangle^2)/2 = 1.10|\langle \boldsymbol{u} \rangle|^2$, whereas at a Reynolds number of 23.3, $(\langle u_y' \rangle^2 + \langle u_z' \rangle^2)/2 = 1.06|\langle \boldsymbol{u} \rangle|^2$. These results suggest that hydrodynamic dispersion at large Péclet numbers would be less influenced by finite Reynolds numbers at large solid volume fractions than at small solid volume fractions. However, hold-up dispersion, coming from the development of recirculating flow in the narrow gaps between the spheres, would increase the longitudinal component of the effective hydrodynamic diffusivity at moderate Reynolds numbers. Relative to the contribution from mechanical dispersion, which appears not to depend very much on the Reynolds number, the hold-up contribution might be very difficult to measure, since the volume of fluid occupied by stagnant fluid is very small.

5.4. *Transition to unsteady flow*

At many of the largest Reynolds numbers shown in figures 18–24, temporal fluctuations in the average velocity, in at least one of the sphere configurations, were

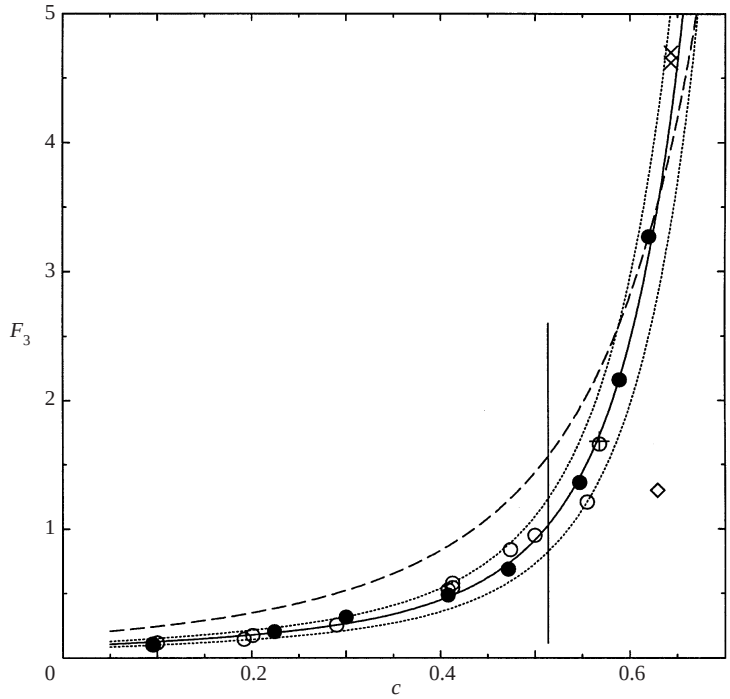

FIGURE 25. The rate at which the non-dimensional drag force on the spheres in random arrays increases with the Reynolds number at moderate Reynolds numbers. The circles are from the lattice-Boltzmann simulations shown in figures 18–24 and listed in table 1. Filled circles identify those simulations, at each nominal solid volume fraction, with the largest sphere radii and the largest number of spheres in the computational domain. The solid line is from (7), which was obtained from all the results identified with both open and filled circles, and the dotted lines indicate deviations up to $\pm 20\%$ from the solid line. The dashed line is from Ergun's correlation (1) (Ergun 1952). The plus symbol is from the lattice-Boltzmann simulations of Maier *et al.* (1998) for flow in a cylindrical packed-bed of spheres with $Re < 6$, and the crosses are from the experiments of Fand *et al.* (1987). The diamond is for a face-centred cubic array with the average pressure gradient directed along the x-axis, and the vertical line shows the range of values obtained for a close-packed simple cubic array with θ_p in the range 0–$\pi/4$.

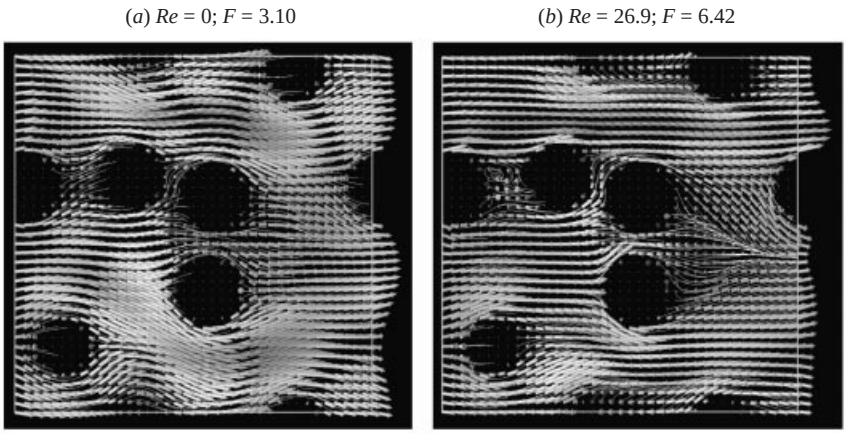

FIGURE 26. Visualizations of (*a*) Stokes flow and (*b*) a moderate-Reynolds-number flow in a random array of spheres with $(c, a, n_s) = (0.0960, 6.8, 32)$.

(*a*) $Re = 0$; $F = 84.5$

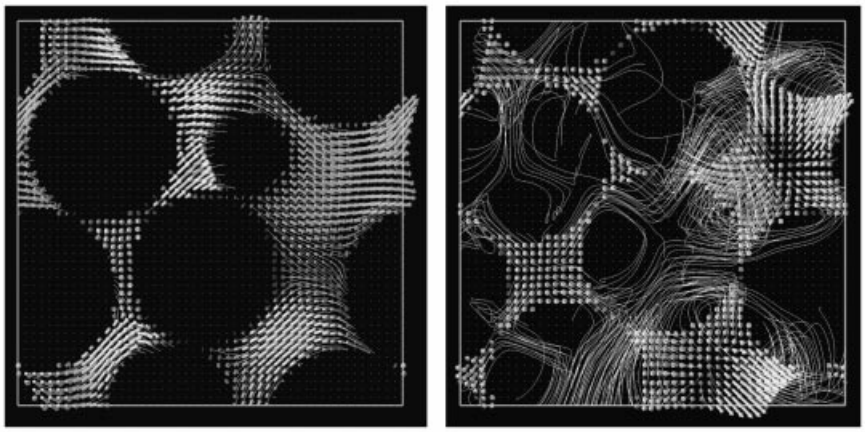

(*b*) $Re = 23.3$; $F = 158$

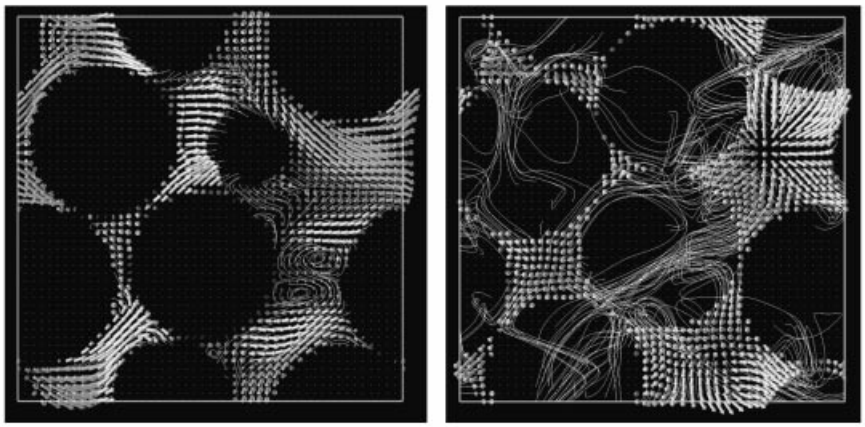

FIGURE 27. Visualizations of (*a*) Stokes flow and (*b*) a moderate-Reynolds-number flow in a random array of spheres with $(c, a, n_s) = (0.588, 19.8, 16)$, where a is in lattice units. In the images on the left the flow is from left to right, whereas in those on the right the flow is out of the page.

observed at long times. The smallest Reynolds numbers at which unsteady flows were observed give an upper bound on the critical Reynolds number, at each solid volume fraction, beyond which unsteady flow persists at long times. These critical Reynolds numbers, Re_c, are listed in table 2 for various solid volume fractions up to the close-packed limit. Note that Re_c does not depend very much on the solid volume fraction, but does tend to be smaller at small and large solid volume fractions. Note also that the critical Reynolds numbers are considerably smaller than that for a single sphere in an unbounded fluid, which, according to the linear stability analysis of Natarajan & Acrivos (1993), is approximately 105.

By observing the dispersion of a dye tracer released from the surface of a single sphere in a close-packed random array of spheres, Jolls & Hanratty (1966) detected unsteady flows at Reynolds numbers in the range 55–75. They also observed the signals from mass-transfer probes located at the sphere surface. Note that the probes require the presence of a mass-transfer boundary layer in order to measure a change in the signal, and hence unsteady flows would be difficult to detect if the fluid velocity fluctuations were sufficiently slow, as when Re is close to Re_c. Therefore,

c	a	n_s	Re_c
0.0960	6.8	32	35
0.192	8.8	16	30
0.201	8.8	16	35
0.290	8.8	16	40
0.408	16.8	16	60
0.472	19.8	64	70
0.479	20.8	16	55
0.474	16.8	60	55
0.500	16.8	16	50
0.536	10.8	16	30
0.547	20.8	64	50
0.555	17.8	16	45
0.620	23.8	64	40
0.633	20.8	32	35
0.641	20.8	16	30

TABLE 2. Approximate upper bounds, obtained from lattice-Boltzmann simulations, on the critical Reynolds number beyond which unsteady flow persists in random arrays of spheres.

these experiments are more likely to over-predict Re_c. Furthermore, it is possible that, at Reynolds numbers close to Re_c, unsteady flow could be localized to disjointed regions of the packed bed. In this case, a range of critical Reynolds numbers might be observed, depending on the position of the test sphere. Since even spatially localized temporal fluctuations in the fluid velocity can be detected in the time series of the spatially averaged velocity from simulations, simulations will tend to give smaller estimates of Re_c. This is indeed the case, since unsteady flows at Reynolds numbers as small as approximately 30 were found from simulations.

The relatively small critical Reynolds numbers that occur at the smaller solid volume fractions can be explained by the random positions of the spheres breaking the symmetry of the flow about any single sphere. Note that breaking of symmetry is also responsible for the transition to unsteady flow past a single sphere in an unbounded fluid (Natarajan & Acrivos 1993). This is consistent with the simulation results for simple cubic arrays, which are steady at considerably larger Reynolds numbers when the flow is directed along the x-axis than when it is directed elsewhere.

The weak dependence of Re_c on the solid volume fraction can be attributed to the following stabilizing and destabilizing influences. First, the velocity in the interstitial region of the arrays is $O((1-c)^{-1})$ larger than the average velocity. However, because the spheres cannot overlap, the largest length scale characterizing the interstitial region of the arrays is $O(a)$. Therefore, the Reynolds number characterizing the stability of the flow in the interstitial region of the arrays is $O(Re/(1-c))$, which can be up to approximately 2.5 times larger than Re. On the other hand, at larger solid volume fractions, the fluid is increasingly confined and, hence, stabilized by neighbouring spheres. Note that the rate of viscous dissipation per unit volume is proportional to $cF\,Re^2$, and hence, for a given Reynolds number, viscous dissipation will be more effective at damping temporal velocity fluctuations at larger solid volume fractions. In other words, the critical Reynolds number tends to be smaller at the smallest and largest solid volume fractions, because at small solid volume fractions longer wavelength disturbances are permitted and there is less viscous dissipation, whereas at larger solid volume fractions larger velocities occur in the small gaps between the spheres, enabling inertia to destabilized shorter wavelength disturbances.

6. Summary

The lattice-Boltzmann method has been used to examine the effects of fluid inertia, at moderate Reynolds numbers, on flows in fixed ordered and random arrays of spheres. Together with the results in the accompanying paper for small but finite Reynolds numbers (Hill *et al.* 2001), this work shows how the drag force on the spheres in ordered and random arrays depends on the Reynolds number at Reynolds numbers from practically zero up to $O(100)$, at solid volume fractions from the dilute limit up to the close-packed limits of the arrays.

The drag force on the spheres in *face-centred cubic* arrays was found to increase when the flow is directed away from the primary axis, whereas in the absence of fluid inertia the drag force is independent of the flow direction. This behaviour was explained by considering the cross-sectional area available for the fluid to traverse in the region between the spheres – in the flow direction – relative to that in the absence of the spheres. When the fluid is forced to flow away from the primary axis, the decrease in the cross-sectional area increases the fluid velocity in the region between the spheres. This increases the difference between the pressures upstream and downstream of the spheres and, hence, increases the drag force. At relatively large solid volume fractions, the non-dimensional drag force was found to increase linearly with the Reynolds number over a wide range of Reynolds numbers. The rate at which it increases was compared to Ergun's correlation for random arrays, which showed that the drag force on the spheres in face-centred cubic arrays is less than in random arrays, irrespective of the flow direction.

For *simple cubic* arrays, the drag force at moderate Reynolds numbers was found to be least when the flow is directed along the primary axis. In contrast to the behaviour at larger solid volume fractions, the drag force on the spheres in dilute arrays, at a given Reynolds number, does not increase monotonically with the angle between the average pressure gradient and the primary axis of symmetry. With increasing solid volume fraction, the velocity fields were shown to increase in complexity and in their dependence on the flow direction. In close-packed arrays, for example, visualizations of fluid velocity fields showed that much of the fluid in the gaps between the spheres, in the flow direction, flows upstream when the flow is directed away from the primary axis. These flows became unsteady at relatively small Reynolds numbers. The drag force on the spheres in dilute simple cubic arrays was found to be smaller than that on a single sphere in an unbounded fluid, and the difference increased with the Reynolds number. This interesting behaviour comes from the long-range interaction of the wakes with downstream spheres, and its effectiveness increases with the Reynolds number because the wakes are able to extend further downstream.

Finally, moderate-Reynolds-number flows in *random* arrays of spheres were examined. The non-dimensional drag force was found to increase linearly with the Reynolds number at Reynolds numbers greater than approximately 40. At smaller Reynolds numbers and larger solid volume fractions, the rate at which the drag force increases with the Reynolds number is closer to that predicted by Ergun's correlation. However, at the largest Reynolds numbers, where the non-dimensional drag force increases linearly with the Reynolds number, the rate at which it increases is considerably smaller than given by Ergun's correlation, particularly at solid volume fractions smaller than those that can be achieved in physical experiments. This difference was explained by the microstructure in packed beds with solid volume fractions less than the close-packed limit being necessarily inhomogeneous at the micro-scale. The difference between the drag force on the spheres in packed beds and random arrays highlights the increasing role that the micro-structure plays at

moderate Reynolds numbers. This was corroborated by the Stokes-flow drag force on the particles in packed beds (physical experiments) and random arrays (simulations) being indistinguishable over the entire range of solid volume fractions that can be achieved in physical experiments.

At a solid volume fraction of 0.096, the variance of the transverse components of the velocity, when scaled with the square of the magnitude of the average velocity, was found to decrease with increasing Reynolds number, because at large Reynolds numbers the fluid's inertia carries it more directly through the arrays. However, at a solid volume fraction of 0.588, the velocity variance scaled with the square of the average velocity was found to be relatively independent of the Reynolds number. This is because the velocity fluctuations at large solid volume fractions are dominated by the fluid having to flow along the tortuous trajectories close to the spheres. These observations suggest that the effect of finite Reynolds numbers on hydrodynamic dispersion at large Péclet numbers would be to decrease the transverse components of the effective hydrodynamic diffusivity relative to that of a Stokes flow, particularly at small solid volume fractions.

The random positions of the spheres was shown to give rise to unsteady flow at much smaller Reynolds numbers than for a single sphere in an unbounded fluid. Steady flow was suggested to be destabilized by (i) the breaking of symmetry about any single sphere due to the velocity disturbances produced by the other spheres, (ii) the longer wavelength disturbances that are allowed to develop with decreasing solid volume fraction, (iii) the decreasing rate of viscous dissipation with decreasing solid volume fraction, and (iv) the large velocities that occur in the small gaps between the spheres when the solid volume fraction is large. Consequently, the critical Reynolds number does not vary significantly with the solid volume fraction, but it does tend to be smaller at the smallest and largest solid volume fractions.

This work was funded by the National Science Foundation (NSF) under grant number CTS-9526149, and the computations were performed using the resources of the Cornell Theory Center. We would also like to thank Alexander Boyarski for his assistance in producing the three-dimensional flow visualizations and Alexander Z. Zinchenko for providing close-packed random sphere configurations that were used in this work.

REFERENCES

Andrade, J. S., Almeida, M. P., Mendes Filho, J., Havlin, S., Suki, B. & Stanley, H. E. 1997 Fluid flow through porous media: The role of stagnant zones. *Phys. Rev. Lett.* **79**, 3901–3904.

Batchelor, G. K. 1967 *An Introduction to Fluid Dynamics*. Cambridge University Press.

Carman, P. C. 1937 Fluid flow through a granular bed. *Trans. Inst. Chem. Engrs Lond.* **15**, 150–156.

Clift, R., Grace, J. R. & Weber, M. E. 1978 *Bubbles, Drops, and Particles*. Academic.

Edwards, D. A., Shapiro, M., Bar-Yoseph, P. & Shapira, M. 1990 The influence of Reynolds number upon the apparent permeability of spatially periodic arrays of cylinders. *Phys. Fluids* A **2**, 45–55.

Eidsath, A., Carbonell, R. G. S., Whitaker, S. & Herrmann, L. R. 1983 Dispersion in pulsed systems – iii. Comparison between theory and experiments for packed beds. *Chem. Engng Sci.* **38**, 1803–1816.

Ergun, S. 1952 Fluid flow through packed columns. *Chem. Engng Prog.* **48**, 89–94.

Fand, R. M., Kim, B. Y. K., Lam, A. C. C. & Phan, R. T. 1987 Resistance to the flow of fluids through simple and complex porous media whose matrices are composed of randomly packed spheres. *Trans. ASME: J. Fluids Engng* **109**, 268–274.

Ghaddar, C. K. 1995 On the permeability of unidirectional fibrous media: A parallel computational approach. *Phys. Fluids* **7**, 2563–2586.

Hill, R. J. 2001 The effects of fluid inertia on flows in porous media. PhD thesis, Cornell University.

Hill, R. J., Koch, D. L. & Ladd, A. J. C. 2001 The first effects of fluid inertia on flows in ordered and random arrays of spheres. *J. Fluid Mech.* **448**, 213–241.

Johnson, T. A. & Patel, V. C. 1999 Flow past a sphere up to a Reynolds number of 300. *J. Fluid Mech.* **378**, 19–70.

Jolls, K. R. & Hanratty, T. J. 1966 Transition to turbulence for flow through a dumped bed of spheres. *Chem. Engng Sci.* **21**, 1185–1190.

Koch, D. L. & Brady, J. F. 1985 Dispersion in fixed beds. *J. Fluid Mech.* **154**, 399–427.

Koch, D. L. & Brady J. F. 1989 The effect of order on dispersion in porous media. *J. Fluid Mech.* **200**, 173–188.

Koch, D. L. & Ladd, A. J. C. 1997 Moderate Reynolds number flows through periodic and random arrays of aligned cylinders. *J. Fluid Mech.* **349**, 31–66.

Maier, R. S., Kroll, D. M., Kutovsky, Y. E., Davis, H. T. & Bernard, R. S. 1998 Simulation of flow through bead packs using the lattice-Boltzmann method. *Phys. Fluids* **10**, 60–74.

Nakamura, I.1976 Steady wake behind a sphere. *Phys. Fluids* **19**, 5–8.

Natarajan, R. & Acrivos, A. 1993 The instability of the steady flow past spheres and disks. *J. Fluid Mech.* **254**, 323–344.

Rojas, S. & Koplik, J. 1998 Nonlinear flow in porous media. *Phys. Rev.* E **58**, 4776–4782.

Russel, W. B., Saville, D. A. & Schowalter, W. R. 1989 *Colloidal Dispersions.* Cambridge University Press.

Taneda, S. 1956 Experimental investigation of the wake behind a sphere at low Reynolds numbers. *J. Phys. Soc. Japan* **11**, 1104–1108.

Wegner, T. H., Karabelas, A. J. & Hanratty, T. J. 1971 Visual studies of flow in a regular array of spheres. *Chem. Engng Sci.* **26**, 59–63.

Zinchenko, A. Z. 1994 Algorithm for random close packing of spheres with periodic boundary conditions. *J. Comput. Phys.* **114**, 298–306.